



**FACULTY  
OF MATHEMATICS  
AND PHYSICS**  
Charles University

**BACHELOR THESIS**

Martin Vavřík

**Simulation and Reconstruction  
of Charged Particle Trajectories  
in an Atypic Time Projection Chamber**

Institute of Particle and Nuclear Physics

Supervisor of the bachelor thesis: Mgr. Tomáš Sýkora, Ph.D.

Study programme: Physics

Prague 2025

9 I declare that I carried out this bachelor thesis independently, and only with the  
10 cited sources, literature and other professional sources. It has not been used to  
11 obtain another or the same degree.

12 I understand that my work relates to the rights and obligations under the Act  
13 No. 121/2000 Sb., the Copyright Act, as amended, in particular the fact that the  
14 Charles University has the right to conclude a license agreement on the use of this  
15 work as a school work pursuant to Section 60 subsection 1 of the Copyright Act.

In ..... date .....  
Author's signature



Title: Simulation and Reconstruction of Charged Particle Trajectories in an Atypical Time Projection Chamber Added hyphen to avoid overfull hbox

Author: Martin Vavřík

Institute: Institute of Particle and Nuclear Physics

Supervisor: Mgr. Tomáš Sýkora, Ph.D., Institute of Particle and Nuclear Physics

Abstract: Abstract.

Keywords: key words

# Contents

18	<b>Motivation</b>	<b>2</b>
19	0.1 ATOMKI Anomaly . . . . .	2
20	0.1.1 ATOMKI Measurements . . . . .	2
21	0.1.2 Other Experiments . . . . .	3
22	0.2 X17 Project at IEAP CTU . . . . .	5
23	<b>1 Time Projection Chamber</b>	<b>7</b>
24	1.1 Charge transport in gases . . . . .	7
25	1.1.1 Drift . . . . .	7
26	1.1.2 Diffusion . . . . .	8
27	1.2 Readout . . . . .	8
28	1.2.1 Multi-Wire Proportional Chamber . . . . .	8
29	1.2.2 Gas Electron Multiplier . . . . .	9
30	1.2.3 Micromegas . . . . .	9
31	1.2.4 Parallel Plate Chamber . . . . .	9
32	1.3 Orthogonal Fields TPC at IEAP CTU . . . . .	9
33	1.3.1 Coordinate Systems . . . . .	9
34	1.3.2 Magnetic Field Simulation . . . . .	11
35	<b>2 Track Simulation</b>	<b>13</b>
36	2.1 Microscopic Simulation . . . . .	13
37	2.2 Runge-Kutta Simulation . . . . .	14
38	<b>3 Track Reconstruction</b>	<b>15</b>
39	3.1 Reconstruction Assuming Steady Drift . . . . .	15
40	3.2 Ionization Electron Map . . . . .	17
41	3.2.1 Gradient Descent Search . . . . .	20
42	3.2.2 Interpolation on the Inverse Grid . . . . .	21
43	3.3 Discrete Reconstruction . . . . .	22
44	<b>4 Energy Reconstruction</b>	<b>24</b>
45	4.1 Cubic Spline Fit . . . . .	24
46	4.2 Circle and Lines Fit . . . . .	26
47	4.2.1 Two-dimensional fit . . . . .	26
48	4.2.2 Three-dimensional fit . . . . .	28
49	4.3 Runge-Kutta Fit . . . . .	28
50	<b>Conclusion</b>	<b>30</b>
51	<b>Bibliography</b>	<b>32</b>
52	<b>List of Figures</b>	<b>35</b>
53	<b>List of Tables</b>	<b>37</b>
54	<b>List of Abbreviations</b>	<b>38</b>

# Motivation

A Time Projection Chamber (TPC) is a type of gaseous detector that detects charged particle trajectories by measuring the positions and drift time of ions created in the gas; details are provided in Section 1. The energy of these particles can be inferred from the curvature of their trajectory in the magnetic field.

The goal of this thesis is to develop an algorithm for the reconstruction of charged particle trajectories and energy in an atypic TPC with orthogonal electric and magnetic fields, hereafter referred to as the Orthogonal Fields TPC (OFTPC), used in the X17 project at the Institute of Experimental and Applied Physics, Czech Technical University in Prague (IEAP CTU). Furthermore, we present the results of testing this algorithm with different samples of simulated data. (We use the Garfield++ toolkit [1] for simulations in combination with the ROOT framework [2] for data analysis and visualization. Some of our more demanding simulations are run on the MetaCentrum grid [3].)

The X17 project in IEAP CTU aims to reproduce measurements of anomalous behavior in the angular correlation distribution of pairs produced by the Internal Pair Creation (IPC) mechanism [4] during the decay of certain excited nuclei ( $^8\text{Be}$ ,  $^{12}\text{C}$ , and  $^4\text{He}$ ) observed by a team at ATOMKI in Hungary. **I would leave this here as a short summary before I explain it in more detail in the sections below.**

**Add citations: X17 project, VdG. Maybe also TPC, etc.**

## 0.1 ATOMKI Anomaly

Many theories propose the existence of new light bosons that are weakly coupled to ordinary matter [5]. These particles are potential dark matter candidates and could solve other issues with the Standard Model, such as the strong CP problem and the anomalous muon magnetic moment.

A possible way of detecting such bosons with a short lifetime is to observe nuclear transitions of excited nuclei. If a boson was emitted during the transition and subsequently decayed into an electron-positron pair, we could observe this as a peak on top of the  $e^+e^-$  angular correlation from IPC and External Pair Creation (EPC).

### 0.1.1 ATOMKI Measurements

Previously, there were several measurements of IPC in nuclear transitions in  $^8\text{Be}$  at Institute für Kernphysik (Frankfurt) [6, 7, 8] and at ATOMKI [9, 10] resulting in different anomalies with invariant mass in the range 5–15 MeV. This prompted a development of a better spectrometer.

In 2015, a group at ATOMKI led by Attila Krasznahorkay observed an anomalous IPC in  $^8\text{Be}$  [11]. They used the  $^7\text{Li}(p, \gamma)^8\text{Be}$  reaction at the  $E_p = 1030$  keV proton capture resonance to prepare the 18.15 MeV excited state ( $J^\pi = 1^+$ ,  $T = 0$ ). This state decays predominantly through M1 transitions to the ground state ( $J^\pi = 0^+$ ,  $T = 0$ ) and to the 3.03 MeV state ( $J^\pi = 2^+$ ,  $T = 0$ ) [12].

96 The angular correlation of the  $e^+e^-$  pairs created internally in these transitions  
 97 were measured and compared to the simulation; results from a narrow  $E_{\text{sum}} =$   
 98  $= 18$  MeV region are shown in Figure 1a. The simulation includes boson decay  
 99 pairs for different boson masses. The disparity parameter  $y$  is defined as

$$y = \frac{E_{e^-} - E_{e^+}}{E_{e^-} + E_{e^+}}, \quad (1)$$

100 where  $E_{e^-}$  and  $E_{e^+}$  are the kinetic energies of the electron and positron.

101 Their experimental setup was later upgraded ([details?](#)) and used for new mea-  
 102 surements. In 2022 the  $^8\text{Be}$  anomaly was also measured using the  $E_p = 441$  keV  
 103 resonance to produce the 17.64 MeV excited state ( $J^\pi = 1^+$ ,  $T = 1$ ) which again  
 104 decays primarily to the ground state and the 3.03 MeV state [12]. The anomaly  
 105 was also measured for  $E_p = 650$  and 800 keV where E1 transitions from the direct  
 106 proton capture dominate [13]. The results for  $e^+e^-$  with  $E_{\text{sum}} \in [13.5, 20]$  MeV  
 107 are shown in Figure 1b.

108 The newer setup was also used in 2021 to study the  $^3\text{H}(p, e^+e^-)^4\text{He}$  reaction at  
 109  $E_p = 510, 610$  and 900 keV [14], inducing direct and resonant capture populating  
 110 the overlapping first 20.21 MeV ( $J^\pi = 0^+$ ) and second 21.01 MeV ( $J^\pi = 0^-$ )  
 111 excited states [15]. The comparison of simulated and measured  $e^+e^-$  pair angular  
 112 correlations in the  $E_{\text{sum}} \in [18, 22]$  MeV region is shown in Figure 1c.

113 In 2022, another anomaly was measured in the  $^{11}\text{B}(p, e^+e^-)^{12}\text{C}$  process [16].  
 114 The  $E_p = 1388$  keV resonance was used to populate the 17.23 MeV excited state  
 115 ( $J^\pi = 1^+$ ,  $T = 1$ ) with a large width  $\Gamma = 1.15$  MeV [17]. This state decays  
 116 mainly through E1 transitions to the ground state  $J^\pi = 0^+$  and to the 4.44 MeV  
 117 state  $J^\pi = 2^+$ . To compensate for energy losses in the target, five energies in  
 118 the range  $E_p = 1.5\text{--}2.5$  MeV were used. The experimental angular correlation for  
 119 the 17.23 MeV transition to the ground state is shown in Figure 1d.

120 Possible explanations of the anomaly include experimental effects, higher or-  
 121 der processes in the Standard Model [18, 19] or even a protophobic fifth force  
 122 mediated by a new 17 MeV boson X17 [20]. [Zhang and Miller: https://www.](#)  
 123 [sciencedirect.com/science/article/pii/S0370269321000010](#)

## 124 0.1.2 Other Experiments

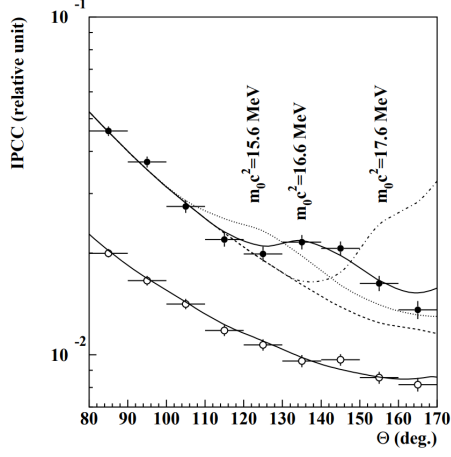
125 Since the ATOMKI measurements, several experiments have been initiated to  
 126 attempt to replicate the results and search for the hypothetical X17 particle.  
 127 [Here are a few with results. Could cite the ATOMKI review paper here.](#)

### 128 Two-arm $e^+e^-$ spectrometer in Hanoi

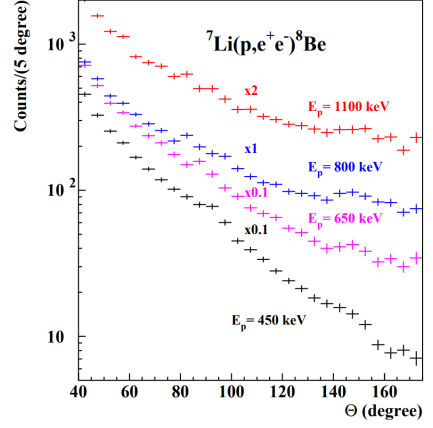
129 The anomaly in  $^8\text{Be}$  has been observed with  $> 4\sigma$  confidence by a team at the  
 130 Hanoi University of Sciences for  $E_p = 1225$  keV [21]. They built a two-arm  
 131 spectrometer in collaboration with ATOMKI and calibrated it using the 17.6 MeV  
 132 M1 transition. The results are shown in Figure 2.

### 133 Collisions at Nuclotron in Dubna

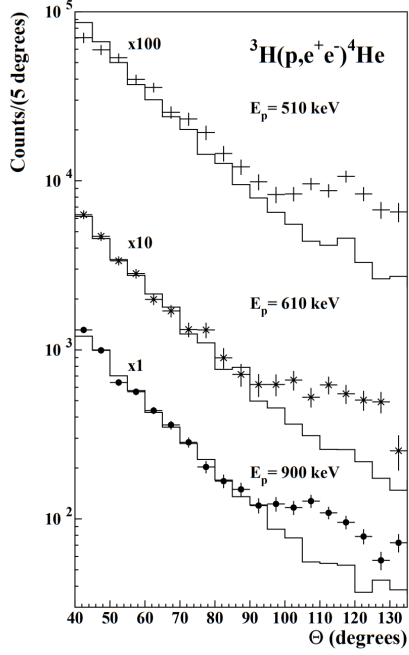
134 At the Joint Institute for Nuclear Research in Dubna, signal in the form of en-  
 135 hanced structures in the  $\gamma\gamma$  spectra at  $\sim 17$  and  $\sim 38$  MeV invariant masses



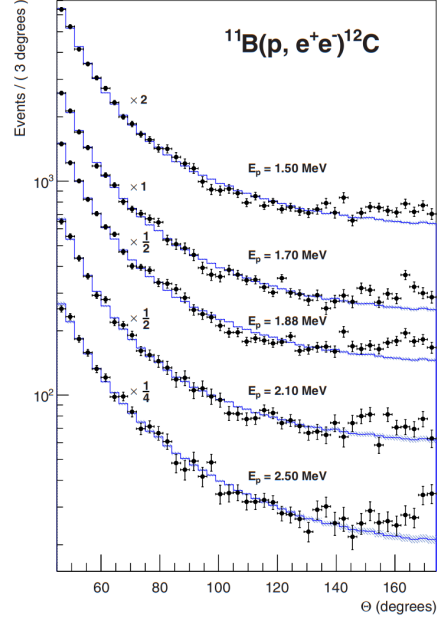
(a) Experimental  $e^+e^-$  pair correlations measured in the  ${}^7\text{Li}(p, e^+e^-){}^8\text{Be}$  reaction with  $|y| \leq 0.5$  (closed circles) and  $|y| \geq 0.5$  (open circles) [11].



(b) Experimental  $e^+e^-$  pair correlations measured in the  ${}^7\text{Li}(p, e^+e^-){}^8\text{Be}$  reaction with the improved setup for different proton beam energies [13].



(c) Experimental  $e^+e^-$  pair correlations measured in the  ${}^3\text{H}(p, e^+e^-){}^4\text{He}$  reaction with  $|y| \leq 0.3$  for different proton beam energies [14].



(d) Experimental  $e^+e^-$  pair correlations measured in the  ${}^{11}\text{B}(p, e^+e^-){}^{12}\text{C}$  reaction for different proton beam energies [16].

Figure 1: The ATOMKI anomalous IPC measured for different nuclei.



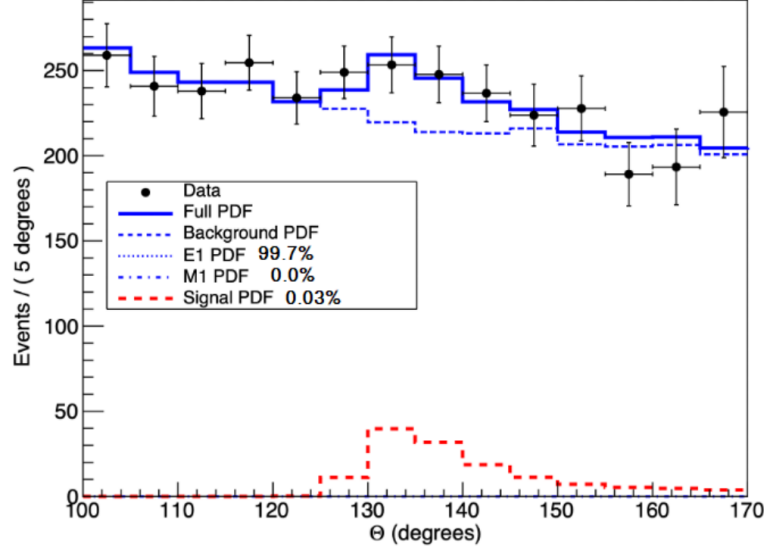


Figure 2: Results from the Hanoi spectrometer – angular  $e^+e^-$  pair correlations measured in the  ${}^7\text{Li}(p, e^+e^-){}^8\text{Be}$  reaction at  $E_p = 1225$  keV [21].

for  $p + \text{C}$ ,  $d + \text{C}$  and  $d + \text{Cu}$  reactions at momenta 5.5, 2.75, and 3.83 GeV per nucleon [22]. Monte Carlo simulations support the conclusion that the signals are a consequence of a decay of unknown particles X17 and E38.

### The MEG II (Muon Electron Gamma) experiment

Experiments using the  ${}^7\text{Li}(p, e^+e^-){}^8\text{Be}$  reaction were carried out at the Paul Scherrer Institute with the MEG II superconducting solenoid spectrometer [23]. Analysis of the data with  $E_p = 1080$  keV exciting both of the resonances (beam fully stopping in the target) found no significant evidence supporting the X17 hypothesis, results are shown in Figure 3. An upper bound (at 90% confidence) on the X17-to- $\gamma$  branching ratio was set at  $1.2 \cdot 10^{-5}$  for the 18.15 MeV state (larger than the ratio  $5.8 \cdot 10^{-6}$  obtained by ATOMKI in 2016). Could add their 90% C.L bounds figure also.

## 0.2 X17 Project at IEAP CTU

The aim of the X17 project at the Van der Graaff facility of the Institute of Experimental and Applied Physics, Czech Technical University in Prague is to repeat the original ATOMKI experiments with  ${}^7\text{Li}$  and  ${}^3\text{H}$  targets using an independent  $e^+e^-$  spectrometer. In order to effectively measure the anomaly, we need to reconstruct both the energy and the angular correlation of the  $e^+e^-$  pairs. The spectrometer will use three layers of detectors to achieve this – Timepix 3 (Tpx3) silicon pixel detector and Multi-Wire Proportional Chamber (MWPC) layers for the angle reconstruction and a Time Projection Chamber (TPC) layer for the energy reconstruction. Spectrometer CAD drawing (coordinates here or next chapter?). Cite some VdG paper, mention grant? Using [https://cernbox.cern.ch/pdf-viewer/public/rf0oU1nqVLN3acZ/LuzH\\_submitted.pdf](https://cernbox.cern.ch/pdf-viewer/public/rf0oU1nqVLN3acZ/LuzH_submitted.pdf).

The energy of  $e^+e^-$  pair produced in the reaction is given by the energy

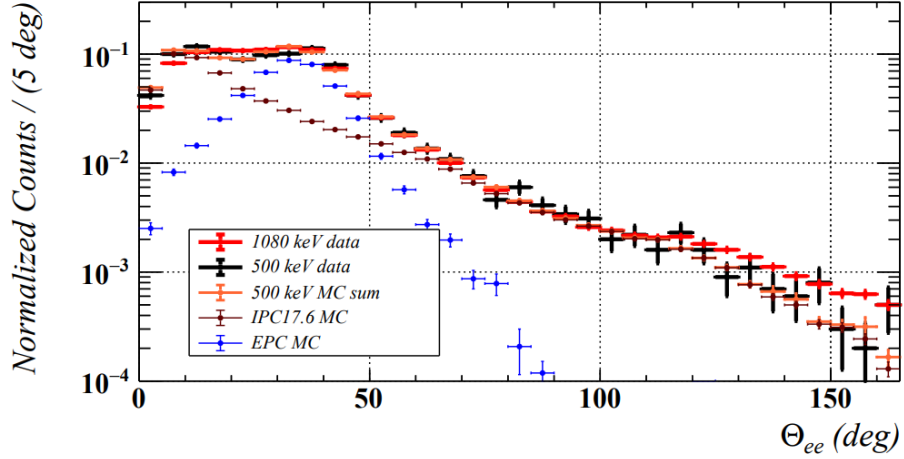


Figure 3: Results from the MEG II experiments – angular correlation of  $e^+e^-$  pairs with  $E_{\text{sum}} \in [16, 20]$  MeV measured in the  ${}^7\text{Li}(p, e^+e^-){}^8\text{Be}$  reaction with proton beam energies 500 and 1080 keV. The 500 keV dataset is fitted with Monte Carlo of both the IPC deexcitation and the EPC produced by gammas [23].

161 available  $E_r$  in the reaction and can be distributed between them arbitrarily.  
 162 Nonetheless in the decay of the hypothetical X17 particle, electron and positron  
 163 should have similar energy and we can therefore use a disparity cut  $|y| \leq 0.5$  for  
 164 the disparity parameter (defined in Equation 1). Interesting events should rarely  
 165 have a particle with an energy below  $E_r/4$  (roughly 4 MeV). Electrons with such  
 166 low energies are scattered significantly by even a thin layer of relatively light  
 167 material, for this reason the Tpx3 layer will be inside of the vacuum tube and the  
 168 tube will have a thinned aluminum segment or Kapton<sup>TM</sup> windows.

169 Tpx3 can measure (in each  $55 \times 55 \mu\text{m}$  pixel of its  $256 \times 256$  grid) time-of-arrival  
 170 (ToA) with 1.6 ns precision and time-over-threshold (ToT) which reflects the de-  
 171 posited energy. This potentially allows 3D tracking if we increase the chip thick-  
 172 ness at the cost of increased scattering. The layer can reconstruct the reaction  
 173 vertex and the angular correlation with high precision.

174 The layer of MWPCs with sensitive area  $40 \times 38 \text{ mm}^2$  will be outside of  
 175 the beam pipe. It will provide an extra point on the particle trajectory which can  
 176 help with the estimation of the reaction vertex and improve the TPC performance  
 177 by providing its entry point.

178 The TPCs, which are a subject of this theses, are in a magnetic field of per-  
 179 manent magnets positioned between them and provide 3D track reconstruction  
 180 and subsequent momentum and particle identification (its charge, or even type  
 181 based on its stopping power). They avoid radiative losses thanks to the small  
 182 interaction with the incident particle. For the readout, triple Gas Electron Mul-  
 183 tiplier (GEM) will be used. The magnetic field layout in our TPCs is atypical –  
 184 orthogonal to the electric field inside the chamber, this is why we call them Or-  
 185 thogonal Fields TPC (OFTPC). Further details about our OFTPCs are provided  
 186 in section 1.3.

# 1. Time Projection Chamber

Using (2010 – a little old) <https://cds.cern.ch/record/1302071/files/CERN-PH-EP-2010-047.pdf>

A Time Projection Chamber (TPC) is a type of gaseous detector that uses the drift in an electric field of free charges (electrons and cations) produced by an ionizing particle to reconstruct its 3D trajectory. When placed inside a magnetic field, the momentum of the incident particle can be inferred from the curvature of its trajectory. Particle identification is also possible using the ionization energy loss inside the TPC.

The original TPC used in the PEP-4 experiment at SLAC was a  $2 \times 2$  m cylinder with a central cathode that produced a strong electric field, making the ionization electrons drift towards one of the bases. The readout consisted of MWPCs, where electrons are accelerated towards the anode wires enough to further ionize the gas and cause an avalanche. **Figure?**

When a charged particle crosses the volume of a TPC, it loses energy by excitation and ionization of the detector gas. Most ionizing collision produce a single ionization electron, sometimes a few secondary electrons are produced close to the collision vertex. In rare cases, the ionization electron has energy large enough to create a measurable track, such an electron is called a  $\delta$ -electron.

**CERES/NA45 – very inhomogeneous magnetic field**

## 1.1 Charge transport in gases

### 1.1.1 Drift

The produced ionization electrons are accelerated towards the readout by the electric field inside the chamber. At the same time, they lose speed by colliding with the gas particles, quickly reaching a constant (for a given field  $\mathbf{E}, \mathbf{B}$ ) mean drift velocity. The electrons might be absorbed by electronegative impurities, such as halides and oxygen.

In many gases (called "hot", e.g., Ar or  $\text{CH}_4$ ), the drift velocity is much greater than that of their thermal motion thanks to a high proportion of elastic collisions. On the other hand, "cold" gases like  $\text{CO}_2$  have a higher proportion of inelastic collisions (e.g., thanks to the excitation of rotational and vibrational states) and therefore much lower drift velocity.

The cations produced by the ionization lose a significant portion of their energy during each collision thanks to their large mass. This makes their drift velocity much smaller and their energy is close to thermal. Since their momentum isn't randomized to such extent during collisions, their diffusion is smaller.

The drift is also influenced by the magnetic field, Langevin derived a good approximation for the drift velocity vector:

$$\mathbf{v}_d = \left( \frac{\mathbf{E}}{\|\mathbf{E}\|} + \omega\tau \frac{\mathbf{E} \times \mathbf{B}}{\|\mathbf{E}\|\|\mathbf{B}\|} + \omega^2\tau^2 \frac{\mathbf{E} \cdot \mathbf{B}}{\|\mathbf{E}\|\|\mathbf{B}\|} \cdot \frac{\mathbf{B}}{\|\mathbf{B}\|} \right) \frac{q\tau}{m(1 + \omega^2\tau^2)} \|\mathbf{E}\|, \quad (1.1)$$

where  $q$  is the charge of the particle,  $m$  is its mass,  $\tau$  is the mean time between collisions and  $\omega = \frac{q}{m}\|\mathbf{B}\|$ . In a standard TPC,  $\mathbf{E}$  is nearly parallel to  $\mathbf{B}$  and

only small corrections are needed. The ion drift is only negligibly influenced by the magnetic field ( $\omega\tau \sim 10^{-4}$  is small). **Lorentz angle for orthogonal fields**  $\tan \psi = -\omega\tau$  (deviation from electric field) – maybe mention in the OFTPC section.

### 1.1.2 Diffusion

Due to random collisions a point-like cloud of electrons or ions will show a Gaussian density distribution at time  $t$  due to the drift in electric field  $\mathbf{E} = (0, 0, E_z)$ :

$$\rho(x, y, z, t) = (4\pi Dt)^{-\frac{3}{2}} \exp\left(-\frac{x^2 + y^2 + (z - v_d t)^2}{4Dt}\right), \quad (1.2)$$

where  $D$  is the diffusion coefficient given by

$$D = \frac{\lambda^2}{3\tau} = \frac{\lambda v_d}{3} = \frac{v_d^2 \tau}{3} = \frac{2\varepsilon\tau}{3m}, \quad (1.3)$$

where  $\lambda$  is the mean free path and  $\varepsilon$  the mean energy. The lateral diffusion width  $\sigma_x$  after a drift distance  $L$  can be expressed as

$$\sigma_x^2 = 2Dt = \frac{4\varepsilon L}{3qE}. \quad (1.4)$$

The minimal diffusion width is given by lowest possible (thermal) energy of the particles  $\varepsilon_{\text{th}} = \frac{3}{2}kT$ :

$$\sigma_{x, \text{min}}^2 = \frac{2kTL}{qE}. \quad (1.5)$$

For electrons in "cold gases" (e.g., Ar/CO<sub>2</sub> mixture), the diffusion approaches this limit up to a certain field intensity ( $\sim 100$  V/cm at 1 atm pressure). **For us 0.45 mm, quite close to the actual diffusion 0.5-0.7 mm.** In reality, the transversal diffusion of electrons can be significantly different from their longitudinal diffusion, simulations are necessary to achieve a precise calculation.

In most TPCs, the transversal (but not the longitudinal) diffusion is reduced by the magnetic field (parallel to electric):

$$\frac{D_T(B)}{D_T(0)} = \frac{1}{C + \omega^2 \tau_2^2}, \quad (1.6)$$

where  $C$  and  $\tau_2$  are parameters dependent on the gas.

## 1.2 Readout

### 1.2.1 Multi-Wire Proportional Chamber

In most (2010 – almost all) TPCs operated in experiments Multi-Wire Proportional Chamber (MWPC) was used for the readout. The electrons enter the chamber through a cathode grid and get accelerated in the strong electric field towards the thin anode wires and create a Townsend avalanche, multiplying the signal. **Alternating with field wires?** The trajectory can be reconstructed using pulses

from each separate wire. Segmented cathode is also often used for the readout of produced cations. Gating grid (reduction of space charge effect, blocking backflow of ions?, closed for electrons  $B=0$ ,  $\Delta V$ , static mode (loss of 25% el.) x opening on trigger)? (gas amplification  $> 10000$  required for good SNR, 100-200 ns shaping time), figure?

## 1.2.2 Gas Electron Multiplier

The Gas Electron Multiplier (GEM) is a thin metal-coated polymer sheet with a high density of small holes. The amplification is achieved by applying voltage on the metal layers, creating a strong electric field inside the holes and causing avalanches. Double or triple stack of GEMs is usually used to create a sufficient gain. From the last foil, the electrons drift to a segmented anode where the signal is read. The backflow of cations is reduced compared to MWPC. Picture of Garfield simulation. Parameters?

## 1.2.3 Micromegas

In a MICRO-MEsh Gaseous Structure (Micromegas) electrons pass through a fine mesh (made out of very thin wires) into the narrow amplification gap where they are multiplied in the high field and read as signal on the segmented anode. Very high field (30-80 kV/cm<sup>2</sup>) is necessary to achieve sufficient gain. Cation backflow is heavily suppressed by the mesh.

## 1.2.4 Parallel Plate Chamber

...

# 1.3 Orthogonal Fields TPC at IEAP CTU

Short description of our detector. Why we use an atypic TPC (benefits, complications). Gas mixture used in the detector (70/30) and its effect.

## 1.3.1 Coordinate Systems

In order to describe events in our detector, we use three distinct spaces: the detector space  $\mathcal{D}$ , the readout space  $\mathcal{R}$  and the pad space  $\mathcal{P}$ . Each space is later used to represent ionization electrons at different stages of the detection process: their creation in the gas, their final position when hitting the readout plane, and finally their representation in the discrete pad space.

### Detector Space

The detector space  $\mathcal{D}$  represents the physical space of our detector. We describe it using Cartesian coordinates  $(x, y, z)$ . The  $z$ -axis is the detector's axis of symmetry, with its negative direction aligned with the proton beam. The origin  $(0, 0, 0)$  is located at the center of the irradiated target. The positive  $x$ -axis passes through the center of one of the OFTPCs along the intersection of its two planes

of symmetry. The  $y$ -axis is then chosen to maintain a right-handed coordinate system.

Since the detector has a hexagonal symmetry, we use only one of its sectors in this work – the first sector  $\mathcal{D}_1 \subset \mathcal{D}$  which is defined by the condition:

$$(x, y, z) \in \mathcal{D}_1 \Leftrightarrow |y| \leq x \tan \frac{\pi}{6}. \quad (1.7)$$

Simulations in this sector can be applied to all sectors by rotating the coordinates accordingly. The volume of the OFTPC in this sector, which has the shape of a trapezoidal prism, has these boundaries:

$$x \in [x_{\min}, x_{\max}] = [6.51, 14.61] \text{ cm}, \quad (1.8)$$

$$z \in [z_{\min}, z_{\max}] = [-8, 8] \text{ cm}, \quad (1.9)$$

$$y_{\max}(x_{\min}) = -y_{\min}(x_{\min}) = 2.75 \text{ cm}, \quad (1.10)$$

$$y_{\max}(x_{\max}) = -y_{\min}(x_{\max}) = 7.45 \text{ cm}, \quad (1.11)$$

where  $y_{\max}(x)$  is the maximal value of the  $y$ -coordinate for a given  $x$ . The readout is located at  $z = 8$  cm; for some purposes, we also define the distance to the readout  $d_r = 8 \text{ cm} - z$  as an alternative to the  $z$ -coordinate. **Keeping this paragraph as it is because the OFTPC volume is distinct from the first sector and some parts of this thesis use the space beyond this volume.**

## Readout Space

The readout space  $\mathcal{R}$  represents the drift time and final positions of ionization electrons as measured by an ideal continuous readout. We describe it using coordinates  $(x', y', t)$ , where  $x'$  and  $y'$  correspond to the detector coordinates at the readout plane ( $z = 8$  cm). **Currently not entirely sure how to put this into a figure since only  $x'$  and  $y'$  correspond to the detector coordinates. The drift time  $t$  is approximately proportional to  $d_r$ .**

## Pad Space

The pad space  $\mathcal{P}$  represents the time bin and pad number of ionization electrons as measured by an ideal discrete readout. **It is not really a subspace of  $\mathcal{R}$  but there is a mapping from  $\mathcal{R}$  to  $\mathcal{P}$ . It is a discretization of a part of  $\mathcal{R}$ , the mapping can be adjusted depending on the simulation. If we assume uniform electric field there will be gaps, we don't use gaps in the reconstruction since the electrons should be pulled towards the pads.**

The readout of the OFTPC will consist (**is the design final?**) of 128 rectangular pads arranged in a staggered pattern (**add image where all the parameters are marked**). Most of the pads are  $0.6 \times 0.9$  cm, only pads 102 and 124 are  $0.6 \times 0.6$  cm, pad 127 is  $0.6 \times 0.509$  cm. The distance of neighboring pads is 0.08 cm, staggering offset is 0.3946 cm.

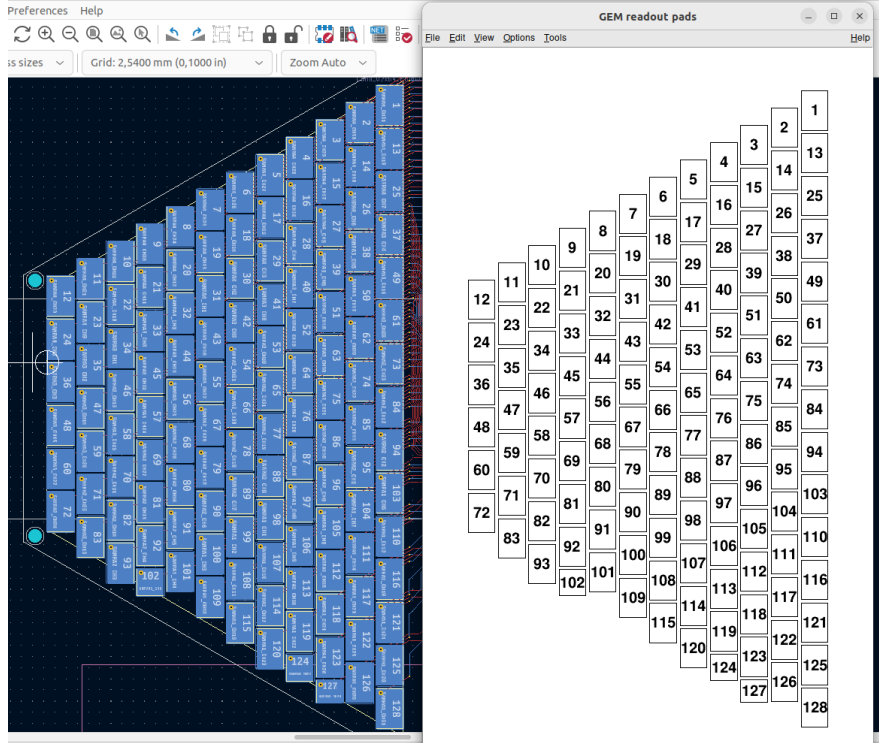


Figure 1.1: Pad layout of the TPC. **Swap for better image.**

### 1.3.2 Magnetic Field Simulation

Magnetic field simulations in Maxwell (citation). Some figures. When working with the magnetic field outside the regular grid, we use trilinear interpolation.

#### Trilinear Interpolation

Trilinear interpolation is a 3D generalization of linear interpolation. It can be used to interpolate a function whose values are known on a regular grid with rectangular prism cells. We use this simple method for interpolating the magnetic field, and it is later used in Section 3.2.1 to interpolate the Ionization Electron Map, a key component of our track reconstruction algorithm. In both cases, we use a regular cubic grid (apparently it is also called a Cartesian grid).

Could put a paragraph about linear interpolation here if it is not clear from the equations below.

Let us consider a cell of our regular grid (a cube) with an edge of length  $a$  containing the point  $\mathbf{C} = (x, y, z)$  where we want to interpolate a function  $f: \mathbb{R}^3 \rightarrow \mathbb{R}$ . We know the values of this function at the vertices of the cell  $\mathbf{C}_{ijk} = (x_0 + ia, y_0 + ja, z_0 + ka)$ , where  $i, j, k \in \{0, 1\}$  are indices. We also define the points  $\mathbf{C}_{ij} = (x, y_0 + ia, z_0 + ja)$  and  $\mathbf{C}_i = (x, y, z_0 + ia)$ . Then the interpolated value  $\hat{f}(\mathbf{C})$  can be calculated as a composition of three linear interpolations (see Figure 1.2):

$$\hat{f}(\mathbf{C}_{ij}) = (1 - x_d) f(\mathbf{C}_{0ij}) + x_d f(\mathbf{C}_{1ij}), \quad (1.12)$$

$$\hat{f}(\mathbf{C}_i) = (1 - y_d) \hat{f}(\mathbf{C}_{0i}) + y_d \hat{f}(\mathbf{C}_{1i}), \quad (1.13)$$

$$\hat{f}(\mathbf{C}) = (1 - z_d) \hat{f}(\mathbf{C}_0) + z_d \hat{f}(\mathbf{C}_1), \quad (1.14)$$

where  $x_d$ ,  $y_d$ , and  $z_d$  are given as follows:

$$x_d = \frac{x - x_0}{a}, \quad y_d = \frac{y - y_0}{a}, \quad z_d = \frac{z - z_0}{a}. \quad (1.15)$$

We can also write

$$\hat{f}(\mathbf{C}) = \sum_{i,j,k \in \{0,1\}} t_x^i t_y^j t_z^k f(\mathbf{C}_{ijk}), \quad (1.16)$$

$$t_\alpha \stackrel{\text{def}}{=} \begin{pmatrix} t_\alpha^0 \\ t_\alpha^1 \end{pmatrix} = \begin{pmatrix} 1 - \alpha_d \\ \alpha_d \end{pmatrix}, \quad (1.17)$$

where  $\alpha \in \{x, y, z\}$  is an index. Furthermore, we can write  $\hat{f}(\mathbf{C})$  as a polynomial:

$$\hat{f}(\mathbf{C}) = \sum_{\alpha, \beta, \gamma \in \{0,1\}} \sum_{i=0}^{\alpha} \sum_{j=0}^{\beta} \sum_{k=0}^{\gamma} (-1)^{(\alpha-i)+(\beta-j)+(\gamma-k)} f(\mathbf{C}_{ijk}) x_d^\alpha y_d^\beta z_d^\gamma. \quad (1.18)$$

We take advantage of this form when generalizing trilinear interpolation to irregular grid in section 3.2.2.

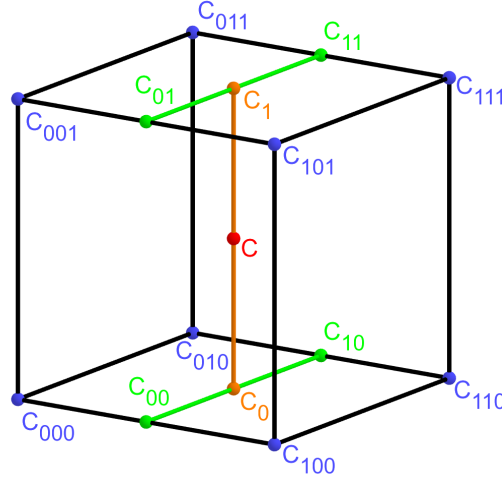


Figure 1.2: Visualization of trilinear interpolation as a composition of linear interpolations. Image drawn in GeoGebra and inspired by a similar image on Wikipedia (which looks a bit worse) – is credit necessary?

Maybe a citation here, although I am not sure it is necessary since it could be considered common knowledge. The last two equations are my own. Maybe  $x_0$ , etc. should be explicitly described.



## 2. Track Simulation

In order to develop and test the reconstruction algorithm, electron and positron tracks are simulated inside the first sector  $\mathcal{D}_1$  of our detector (see Section 1.3.1) with different initial parameters. Two approaches are currently used to simulate tracks, each of them for different purpose.

The **Microscopic Simulation** uses the Garfield++ toolkit [1]. Within this toolkit, the High Energy Electro-Dynamics (HEED) program [24] is used to simulate the primary particle and the class *AvalancheMicroscopic* to simulate the drift of secondary electrons created by ionization in the gas. This is the most precise and time-consuming simulation used; our current goal is to be able to successfully reconstruct its results and determine our best-case energy resolution.

The **Runge-Kutta Simulation** uses the 4th order Runge-Kutta numerical integration (add citation for Runge-Kutta) to simulate the trajectory of the primary particle in the electromagnetic field inside the detector. It is relatively fast since it does not simulate the secondary particles. It is used as part of our reconstruction algorithm and for testing some parts of the reconstruction.

All of these simulations require the knowledge of the electromagnetic field inside the detector. A uniform electric field of  $400 \text{ V}\cdot\text{cm}^{-1}$  is assumed. The magnetic field was simulated in Maxwell (see Section 1.3.2). add citation

Single track in positive x direction or initial parameter randomization. Importance of gas composition, used gas compositions.

### 2.1 Microscopic Simulation

The microscopic simulation, the most detailed simulation used in this work, is performed using the Garfield++ toolkit [1].

The electron transport properties are simulated using the program Magboltz (Add citation.). Two different gas mixtures were used: 90% Ar + 10% CO<sub>2</sub> and 70% Ar + 30% CO<sub>2</sub>. The second mixture will be used in our detector. The temperature is set to 20 °C, the pressure is atmospheric.

The primary track is simulated using the program HEED [24], which is an implementation of the photo-absorption ionization model. This program provides the parameters of ionizing collisions. HEED can also be used to simulate the transport of delta electrons; we do not account for these in the current simulation but plan to include them in the future. The photons created in the atomic relaxation cascade (fluorescence reabsorption, ?) are also not simulated.

Finally, we use the microscopic tracking provided by the class *AvalancheMicroscopic* to simulate the drift of the ionization electrons. Each electron is followed from collision to collision using the equation of motion and the collision rates calculated by Magboltz.

First simulated track in the z direction should be described in detail here (own subsection?). Figures.

Add more detailed and better description of HEED, and microscopic tracking (each their own subsection?). Could also mention Monte Carlo (requires gas file generation - Magboltz) and Runge-Kutta simulation implemented in Garfield,

391 why we don't use them (another subsection? rename the section to Garfield++  
 392 simulation and mention all relevant parts?).

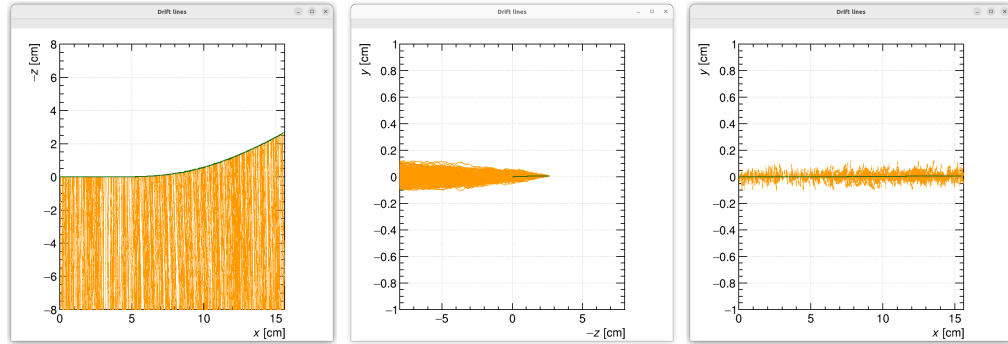


Figure 2.1: Example of a simulated electron track in 70 % argon and 30 % CO<sub>2</sub> atmosphere (on the left). Swap for better images, better zoom. Explain drift lines, primary particle.

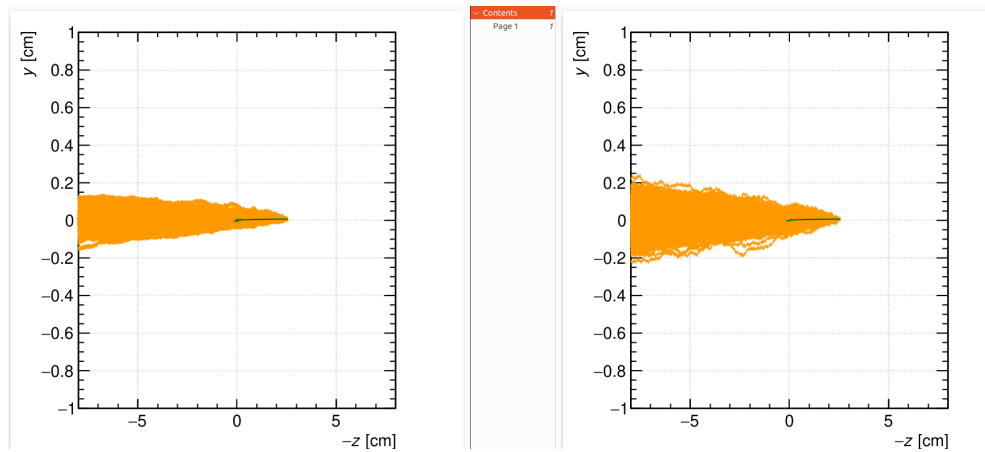


Figure 2.2: Comparison of diffusion in a simulated electron track in 70 % argon, 30 % CO<sub>2</sub> atmosphere and in 90 % argon, 10 % CO<sub>2</sub> atmosphere (on the right). Swap for better image, better zoom. Or put the same pictures for both comparisons in one subfigure, etc. Describe better.

## 393 2.2 Runge-Kutta Simulation

394 Trajectory simulation with 4th order Runge-Kutta. Relativistic equation that is  
 395 numerically integrated by the algorithm.

### 3. Track Reconstruction

In the first stage of the reconstruction algorithm, we reconstruct the track of a primary particle (either an electron or a positron). The result of this step is then used to determine the energy of the particle (Section 4).

The **Reconstruction Assuming Steady Drift** uses the standard TPC approach. With parallel fields, the drift inside a uniform electric field remains undistorted (reference to some future part of the TPC chapter). Therefore, we only need to reconstruct the  $z$ -coordinate from the drift time using the known drift velocity. We also assume that the readout coordinates  $(x', y', t)$  are known exactly, neglecting the pads and time bins.

Reconstruction using the **Ionization Electron Map** (from now on referred to as *the map*) uses a simulation of the drift of secondary (ionization) electrons within the detector volume. This simulation can then be used to interpolate the initial position of the secondary electrons. First attempts neglect the pads.

We use the map for reconstruction in two different ways. The first one uses gradient descent search along with trilinear interpolation (see Section 1.3.2) of the map. The second method uses interpolation on the irregular inverse grid with a linear polynomial.

The **Discrete Reconstruction** uses the map; instead of reconstructing the exact position of each electron, we reconstruct the center of each hit pad with the time corresponding to the midpoint of the time bin. The electron count in each TPC bin (consisting of the pad and the time bin) serves as the charge value, which is then used as a weight in the energy reconstruction fit.

#### 3.1 Reconstruction Assuming Steady Drift

As the first step, we decided to try to reconstruct an electron track with a special set of initial parameters. The origin of the particle is given by the origin of our coordinate system. The initial direction is given by the positive  $x$ -axis. This means the magnetic field of our detector is perpendicular to the momentum of the particle at all times, and we can reduce the problem to two-dimensional space. As an example, we use a track simulated using the microscopic simulation (see Section 2.1) with a kinetic energy of 8 MeV. The gas composition used in this simulation is 90% Ar + 10% CO<sub>2</sub>. Might be better to describe this track in Section 2.1.

In this approach to the reconstruction of the track, we decided to use the common method used in a standard TPC. This will allow us to explore the significance of the atypical behavior in our OFTPC. Additionally, we assume the readout is continuous to further simplify the problem. In this approximation, we reconstruct the initial position of each ionization electron.

The reconstruction is then defined by the following relations between the coordinates of the detector space and the readout space (see Section 1.3.1):

$$x = x', \tag{3.1}$$

$$y = y', \tag{3.2}$$

$$z = v_d t, \tag{3.3}$$

436 where  $v_d$  is the drift velocity of electrons in the given gas mixture. At a phe-  
 437 nomenological level, this velocity can be considered as a function of the electric  
 438 field  $\mathbf{E}$  and the magnetic field  $\mathbf{B}$ :

$$v_d = v_d(\mathbf{E}, \mathbf{B}). \quad (3.4)$$

439 Equation taken from Garfield user manual. The Garfield++ toolkit uses this  
 440 fact to accelerate their drift simulation with non-microscopic approaches (could  
 441 mention in the simulation chapter). Since we assume a uniform electric field in  
 442 our detector and we want to neglect the effect of our unusual magnetic field, we  
 443 consider the drift velocity to be constant in this scenario. We then approximate  
 444 this velocity by fitting the dependence  $z(t)$  taken from the simulated ionization  
 445 electrons. This is in one of the provisional figures. Also, this description is  
 446 not completely accurate; in reality, we fit  $t1:8-y0$  with  $a1*x+a0$  and then invert  
 447 this and use  $8-y0 = b1*t1+b0$  (old coordinates);  $b1=1/a1$  functions as the drift  
 448 velocity. Maybe also define this 8-z variable as an alternative to  $z$  in Section 1.3.1  
 449 and then use it when correcting this.

450 Later, in a commit after this, I plotted some residues (provisional figure),  
 451 which could be useful, but for some reason they are residuals from a spline fit of  
 452 the track?! Probably redo this without the spline fit; just explore the difference  
 453 in individual points.

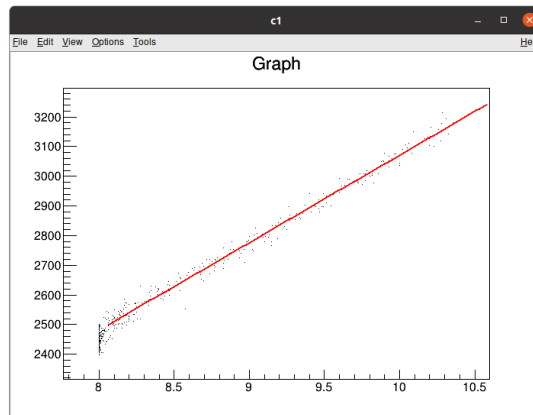


Figure 3.1: Dependence of the drift time on the  $z$  coordinate in 90 % argon and 10 %  $\text{CO}_2$  atmosphere, fitted with a linear function. The fitted function gives us the average drift velocity in the gas and can be used for rough reconstruction in our TPC. Swap for better image with axis labels, etc. Maybe write the fitted equation.

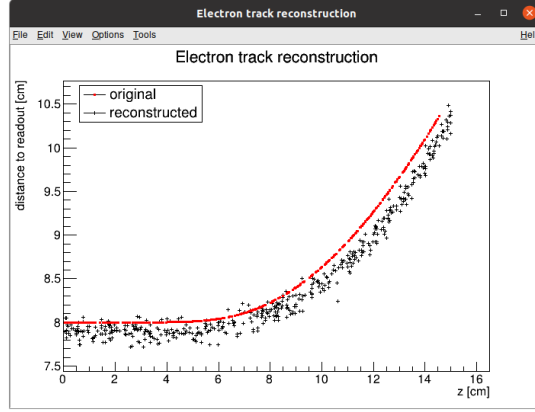


Figure 3.2: First attempt at a track reconstruction using only the drift velocity. This approach works well in a standard TPC (ideally cite some source?). 90 % argon and 10 % CO<sub>2</sub> atmosphere. Swap for better image, correct coordinates.

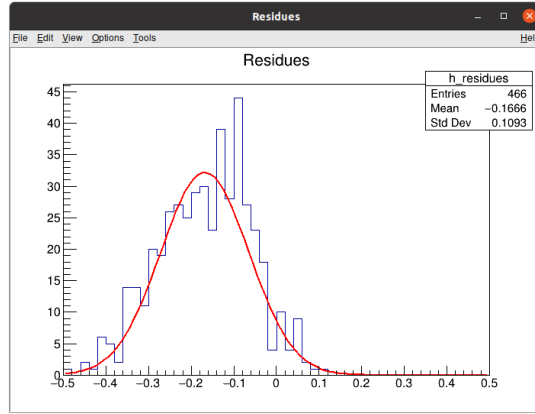


Figure 3.3: First attempt at a track reconstruction using only the drift velocity, residues. Swap for better image, correct coordinates. What's causing the shift? Explain details.

## 3.2 Ionization Electron Map

Inside an OFTPC, the drift of the secondary (ionization) electrons is significantly affected by its magnetic field (pictures of the distortion later, the effect is bigger for the 90/10 composition.). We need to take this into account for accurate reconstruction. In the first approximation, we assume a continuous readout (i.e., we neglect pads). We can then reconstruct the original position of each ionization electron using its readout coordinates. For this purpose, we use the ionization electron map.

The ionization electron map represents a mapping from the detector space to the readout space (see Section 1.3.1). It tells us what readout coordinates  $(x', y', t)$  we can expect on average for an ionization electron created at the detector coordinates  $(x, y, z)$ . More precisely it is a mapping to the distributions on the readout space; we can simplify this as only the means  $\bar{\mathcal{M}}$  and the covariance

467 matrices  $\mathcal{M}_{\text{cov}}$ , assuming Gaussian distribution.

$$\mathcal{M} : \mathcal{D} \longrightarrow \mathcal{R}, (x, y, z) \longmapsto (x', y', t). \quad (3.5)$$

468 To get an approximation of this mapping, we simulate the drift of ionization  
 469 electrons generated on a regular grid inside the volume of our OFTPC <sup>1</sup>. It  
 470 is also useful to simulate multiple (100 in our case) electrons originating from  
 471 the same position so we can get a better information about the average drift  
 472 and its variance. In order to get more accurate results, we use the microscopic  
 473 simulation of these electrons described in Section 2.1. When evaluating the map  
 474 inside the grid, we use trilinear interpolation (see Section 1.3.2). From now on,  
 475 we will denote this interpolated simulation with the same symbol  $\mathcal{M}$ .

476 Finally, we need to invert the map to get the original detector coordinates  
 477  $(x, y, z)$  for the given readout coordinates  $(x', y', t)$ . In our case, we can reason-  
 478 ably assume that the mapping  $\overline{\mathcal{M}}$  is one-to-one (as seen in the simulations). We  
 479 implemented two methods for this purpose: the gradient descent search (Sec-  
 480 tion 3.2.1) and interpolation on the inverse grid (Section 3.2.2).

481 The simulation of the map is a computationally heavy task. For this reason,  
 482 we use the MetaCentrum grid [3] to parallelize needed calculations. At first, this  
 483 was done by evenly distributing the simulated electrons across the individual jobs  
 484 in a simulation with only one electron per vertex in the regular grid with a spacing  
 485 of one centimeter.

486 Later, a more efficient approach was implemented, accounting for the varying  
 487 lengths of the drift of individual electrons. If we index the electrons in the order  
 488 of increasing coordinates  $y, x, z$  (picture?), we can express the number  $n_l$  of full  
 489 XY layers (i.e., electrons with the same  $z$  coordinate) of electrons with index less  
 490 than or equal to  $i$

$$n_l(i) = \left\lfloor \frac{i}{n_{xy}} \right\rfloor, \quad (3.6)$$

491 where  $n_{xy}$  is the number of electrons in each XY layer calculated simply by count-  
 492 ing the electrons that satisfy boundary conditions for  $x$  and  $y$ . These conditions  
 493 should be mentioned above; sector condition + maximal  $x$  value. The number of  
 494 electrons remaining in the top layer is then

$$n_r(i) = i \bmod n_{xy}. \quad (3.7)$$

495 Finally, we can calculate the sum of the drift gaps of electrons up to index  $i$

$$d_{\text{sum}} = (z_{\text{max}} - z_{\text{min}})n_{xy}n_l - \frac{n_l(n_l - 1)}{2}n_{xy}l + n_r(z_{\text{max}} - z_{\text{min}} - n_l l). \quad (3.8)$$

496 We then use a binary search algorithm to find the maximum index  $i$  such that  
 497 the value of this sum is less than the fraction  $\frac{\text{job id}}{\text{max job id}}$  of the total sum. This way  
 498 we obtain the minimal and the maximal index of electrons simulated in the given  
 499 job. The spacing  $l$  should be probably defined above + picture of the simulating  
 500 grid (1 layer). zmin zmax also

501 After the simulation of the map, we calculate the mean readout coordinates  
 502 assuming Gaussian distribution (i.e., we use averages). We also calculate standard

---

<sup>1</sup>we do not take the detector walls into account and simulate even outside of the OFTPC which lets us interpolate even close to the walls

503 deviations in a later commit, should be upgraded to the covariance matrix. We  
 504 never actually plotted the distributions we get when simulating the same electron  
 505 multiple times, so we do not know if our assumptions are accurate (could also  
 506 run some statistical test to see how well the Gaussian distribution fits).

507 The obtained map is then stored in a custom class template *Field*, could  
 508 expand on that. Maybe earlier, since the same template is used for the magnetic  
 509 field.

510 Could insert a table here describing all 4 simulations of the map (gas composi-  
 511 tion, spacing, etc.). Simulation inside of one sector (at first double angle). Extra  
 512 space on the sensor. Edge cases not taken into account (TPC wall). Using qsub  
 513 (not sure if important). Add plots of distortion of the coordinates. Could also do  
 514 these plots in a different way (e.g., drawing all the endpoints of each ionization  
 515 electron or some error ellipse plot).

516 Images to add (comparison of both simulations):

- 517 • 3D visualization of the map, simulation example
- 518 •  $z$  vs.  $t$  plot
- 519 • XY plane distortion for different  $z$  values; with arrows and error bars, for  
 520 all  $z$ -layers with different colors
- 521 • XZ plane ( $y = 0$ ) distortion in  $x$  (maybe not necessary?)
- 522 • XT plot ( $y = 0$ ) showing (small) distortion in drift times

523 More images:

- 524 • Residuals of the continuous readout reconstruction.

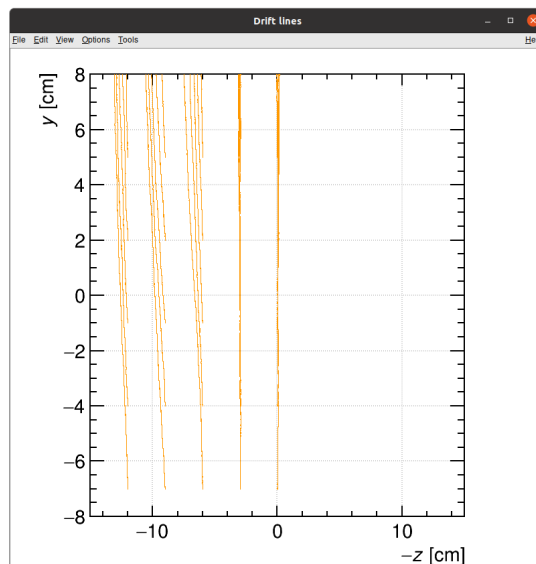


Figure 3.4: Example of map generation. Swap for better image, correct coordinates.

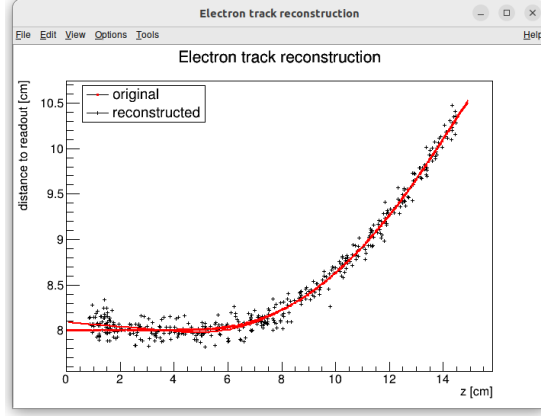


Figure 3.5: Example reconstruction with the map. Swap for better image, correct coordinates.

### 3.2.1 Gradient Descent Search

The first implemented method of reconstruction uses a gradient descent search to calculate an inversion of the map  $\bar{\mathcal{M}}$  in a given point. Gradient descent is an iterative minimization algorithm for multivariate functions. Let  $R \in \mathcal{R}$  be a point in the readout space; we want to find a point  $D = (x, y, z) \in \mathcal{D}$  in the detector space such that

$$\bar{\mathcal{M}}(D) = R = (x'_R, y'_R, t_R). \quad (3.9)$$

We define a function  $f_R$  in the readout space as a distance in this space:

$$f_R(x', y', t) = \sqrt{(x' - x'_R)^2 + (y' - y'_R)^2 + v_d^2(t - t_R)^2}, \quad (3.10)$$

where  $v_d$  is an approximation of the drift velocity in the TPC, obtained from the reconstruction in Section 3.1 (there will be an image with the linear fit there). We make an initial guess (actually in the original code we just take  $z = 0$ ):

$$D_0 = (x'_R, y'_R, v_d t). \quad (3.11)$$

Assuming we have the  $n$ -th estimate  $D_n$ , we calculate the  $i$ -th component of the gradient of  $f_R \circ \bar{\mathcal{M}}$  numerically using central differences:

$$\left[ \nabla(f_R \circ \bar{\mathcal{M}}) \right]^i(D_n) \approx \frac{f_R(\bar{\mathcal{M}}(D_n + s \cdot e^i)) - f_R(\bar{\mathcal{M}}(D_n - s \cdot e^i))}{2s}, \quad (3.12)$$

where  $e^i \in \mathcal{D}$  is the  $i$ -th coordinate vector and  $s$  is the step size. The step size should be sufficiently small; initially, we set it as a fraction of the map's grid spacing  $s = \frac{l}{10}$ . During the minimization, we check that  $f_R(\bar{\mathcal{M}}(D_n)) < 10s$  at all times. When using trilinear interpolation, it would be more efficient to calculate the gradient explicitly ( $\pm$  same result). This could be implemented inside the *Field* template class. The next iteration can be calculated as follows:

$$D_{n+1} = D_n - \gamma \nabla(f_R \circ \bar{\mathcal{M}})(D_n), \quad (3.13)$$

where  $\gamma \in \mathbb{R}^+$  is the damping coefficient. It should be set to a small enough value to ensure convergence, but large enough for sufficient converging speed.



545 The minimization stops either when the error  $f_R(\overline{\mathcal{M}}(D_n))$  drops below a specified  
 546 value or when the number of iterations exceeds a certain limit (in this case,  
 547 a message is printed into the console). The parameters of this method can be  
 548 further optimized (e.g., a better choice of  $\gamma$ , **gradient computation**); instead, we  
 549 later decided to use the interpolation on the inverse grid described in the next  
 550 section.

551 **Measure reconstruction duration and compare it with the inverse grid inter-**  
 552 **polation? Also compare the result? Not sure if this has to be cited.**

### 553 3.2.2 Interpolation on the Inverse Grid

554 **Interpolating between known points in the readout space. Gaussian elimina-**  
 555 **tion, multivariate polynomial. Benefits compared to the gradient descent search**  
 556 **method (one-time computation for the whole map is easy to achieve if needed).**

557 The currently used baseline reconstruction method is the interpolation on  
 558 the inverse grid. Rather than attempting to invert the trilinearly interpolated  
 559 map as in the previous section, we take advantage of the fact that the map  $\overline{\mathcal{M}}$   
 560 is one-to-one (**isomorphism is supposed to preserve structure, not sure how to**  
 561 **interpret that here**). Since we have simulated values of this map on a regular  
 562 grid in the detector space  $\mathcal{D}$ , we also know the inverse map  $\overline{\mathcal{M}}^{-1}$  on the irregular  
 563 inverse grid in the readout space  $\mathcal{R}$ . To get an approximation of the inverse map  
 564 in the entire readout space, we can use interpolation.

565 Since the inverse grid is irregular, trilinear interpolation cannot be applied.  
 566 Given that the simulated map is dense enough to provide a good approxima-  
 567 tion considering the size of our pads, we can adopt a similar approach (more  
 568 complicated and computationally heavy alternative would be natural neighbor  
 569 interpolation). As shown in Equation 1.18 in Section 1.3.2, trilinear interpolation  
 570 can be expressed as a polynomial:

$$\hat{f}(x, y, z) = axyz + bxy + cxz + dyz + ex + fy + gz + h, \quad (3.14)$$

571 where  $a, b, c, d, e, f, g, h$  are coefficients uniquely determined by the values of  
 572 the function at the vertices of the interpolation cell. We can generalize this  
 573 for a function defined on an irregular grid. Given the function values at any eight  
 574 points, we can write a system of eight linear equations

$$\begin{pmatrix} x_1 y_1 z_1 & x_1 y_1 & x_1 z_1 & y_1 z_1 & x_1 & y_1 & z_1 & 1 \\ \vdots & \vdots & \vdots & \vdots & \vdots & \vdots & \vdots & \vdots \\ x_8 y_8 z_8 & x_8 y_8 & x_8 z_8 & y_8 z_8 & x_8 & y_8 & z_8 & 1 \end{pmatrix} \begin{pmatrix} a \\ \vdots \\ h \end{pmatrix} = \begin{pmatrix} f(x_1, y_1, z_1) \\ \vdots \\ f(x_8, y_8, z_8) \end{pmatrix}, \quad (3.15)$$

575 which has a unique solution for the coefficients for most values of  $(x_n, y_n, z_n)$  and  
 576  $f(x_n, y_n, z_n)$ , where  $n \in \{1, \dots, 8\}$ .

577 This approach introduces a small complication: finding the correct pseudo-  
 578 cell (i.e., the image of eight vertices forming a cubic cell in the regular grid) in  
 579 the inverse grid. The eight irregularly spaced vertices of this pseudocell do not  
 580 define a unique volume, so there are multiple possible ways to partition  $\mathcal{R}$  into  
 581 pseudocells, with no obvious choice among them.

582 **We are currently ignoring this problem and performing binary search along**  
 583  **$x, y, z$  (in this order). It shouldn't matter too much because the 70/30 map**

584 doesn't cause such a big distortion and was even accidentally extrapolated for all  
 585  $z$  different from the central plane. Interpolation should be generally faster than  
 586 the gradient descent since we don't need to iterate. We also don't need to optimize  
 587 it to improve performance, if it's too slow we can even calculate the coefficients  
 588 for the entire map before reconstruction.

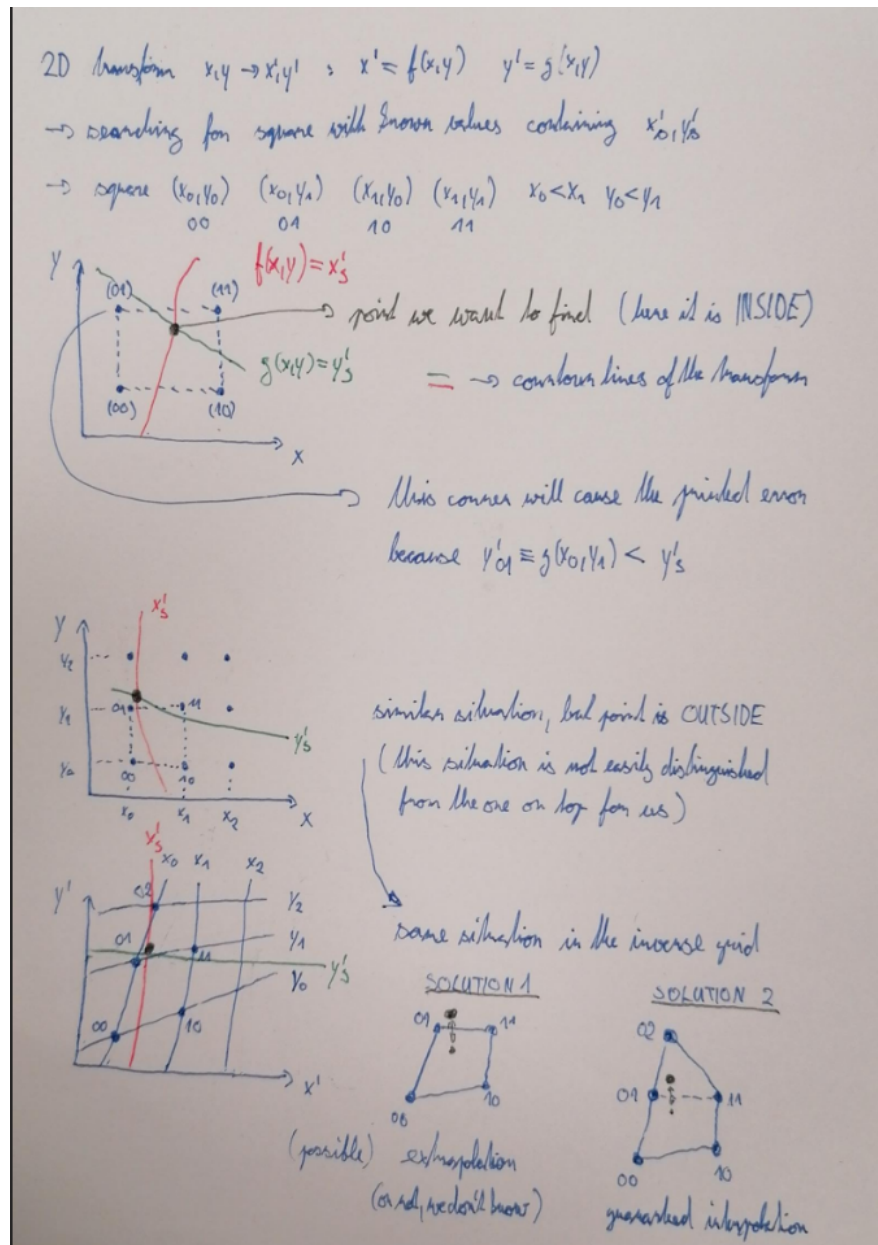


Figure 3.6: Selection of the points for interpolation. Create better images; use the explanation interpolation vs. extrapolation strange property. Solution 2 probably does not make much sense.

### 589 3.3 Discrete Reconstruction

590 Reconstruction with pads and time bins. Maybe testing different pads. Mapping  
 591 the center of the pad (along with the midpoint of the time bin) isn't necessarily

592 the best approach since it might not correspond to the average parameters of  
593 an electron with these readout parameters (insignificant?).

594     It is also possible to make this a subsection of the map, making the previous  
595 subsections parts of a new subsection 'Map Inversion'.

## 4. Energy Reconstruction

The second stage is the reconstruction of the particle's energy using a fit of its reconstructed track (see Section 3). We have tested three ways of reconstructing the energy. Fitting is done using the MINUIT algorithm implemented in ROOT [2]. **Cite some CERN article directly on MINUIT, can add a section.**

The **Cubic Spline Fit** is a tested and later rejected method of energy reconstruction. It uses smoothly connected piecewise cubic polynomials between uniformly spaced nodes. Energy is calculated using the fit parameters by computing the radius of curvature in different points of the fitted curve using the known magnitude of the magnetic field perpendicular to the trajectory. We rejected this method because tuning of the fit to have a reasonably stable radius of curvature turned out to be impractical.

The **Circle and Lines Fit** was chosen as an alternative since this corresponds to the shape of a trajectory of a charged particle crossing a finite volume with a homogeneous magnetic field. The energy of the particle can be estimated using the fitted radius and the magnitude of the perpendicular magnetic field in the middle of the TPC.

The **Runge-Kutta Fit** uses the 4th order Runge-Kutta numerical integration described in Section 2.2. Initial parameters of the track (including the particle's energy) are optimized so that the integrated trajectory fits to the reconstructed one. This fit can also be performed as a single parameter (i.e., energy) fit if we get the initial position and orientation of the particle on the entrance to the TPC from previous detectors (Tpx3 and MWPC, see Section 0.2).

### 4.1 Cubic Spline Fit

The first attempt to get an early estimate of the kinetic energy of the particle uses a cubic spline fit. We use an electron track starting in the origin of our coordinate system with an initial direction in the positive  $x$  axis. The example track is simulated microscopically (see Section 2.1) with a kinetic energy of 8 MeV in a gas mixture 90% Ar + 10% CO<sub>2</sub> (the same track was used in Section 3.1). **This track should probably be described in the simulation chapter.**

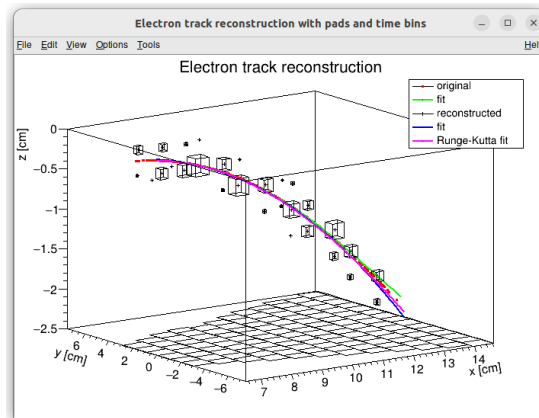


Figure 4.1: Example of a fitted reconstructed track. **Swap for better image.**

626 In order to calculate the spline, we use the class *TSpline3* from ROOT. This  
 627 allows us to evaluate the spline using the coordinates  $(x_n, z_n)$  of each node and  
 628 the derivatives  $d_1, d_2$  in the first and the last node. We can fit these parameters  
 629 of a fixed amount of nodes to the simulated trajectory. We use the IMPROVE  
 630 algorithm provided by the *TMinuit* class in ROOT. This algorithm attempts to  
 631 find a better local minimum after converging.

632 After the fit, we want to get an energy estimate. In order to calculate it, we  
 633 need the radius of curvature, which we get from the fitted spline at every point  
 634 of the trajectory. The part of the spline corresponding to a given node is defined  
 635 as

$$z(x) = z_n + b\Delta x + c(\Delta x)^2 + d(\Delta x)^3, \quad (4.1)$$

636 where  $\Delta x = x - x_n$  and  $b, c, d$  are coefficients. Using this equation, we derive  
 637 the radius of curvature<sup>1</sup> as:

$$r(x) = \frac{(1 + z'^2(x))^{\frac{3}{2}}}{z''(x)} = \frac{(1 + (b + 2c\Delta x + 3d(\Delta x)^2)^2)^{\frac{3}{2}}}{2c + 6d\Delta x}. \quad (4.2)$$

638 Based on the geometry of the detector, we can assume the magnetic field  
 639  $\mathbf{B}(x, 0, z) = (0, B(x, z), 0)$  for a track in the XZ plane. Since the electron is rela-  
 640 tivistic, the effect of the electric field on its trajectory is negligible. The Lorentz  
 641 force  $F_L$  is then always perpendicular to the momentum of the electron and acts  
 642 as a centripetal force  $F_c$ :

$$\mathbf{F}_L = \mathbf{F}_c, \quad (4.3)$$

$$\|e\mathbf{v} \times \mathbf{B}\| = \frac{\gamma m_e v^2}{r}, \quad (4.4)$$

$$ec\beta B = \frac{E_{0e}\beta^2}{r\sqrt{1 - \beta^2}}, \quad (4.5)$$

$$\sqrt{1 - \beta^2} = \frac{E_{0e}\beta}{ecBr}, \quad (4.6)$$

643

$$\beta^2(x) = \left[ 1 + \left( \frac{E_{0e}}{ecB(x, z(x))r(x)} \right)^2 \right]^{-1}, \quad (4.7)$$

644 where  $e$  is the elementary charge,  $c$  is the speed of light in vacuum,  $m_e$  is the rest  
 645 mass of electron,  $E_{0e} = m_e c^2$  is the corresponding energy,  $\gamma$  is the Lorentz factor,  
 646  $\mathbf{v}$  is the velocity of the electron, and  $\beta = \frac{v}{c}$ . We can then finally get our estimate  
 647 of the kinetic energy for a given point on the trajectory as follows:

$$E_{\text{kin}}(x) = \left( \frac{1}{\sqrt{1 - \beta^2(x)}} - 1 \right) E_{0e}. \quad (4.8)$$

648 We can then average these estimates at multiple points to get one final estimate.  
 649 This method was later rejected in favor of the circle and lines fit described in  
 650 Section 4.2. **Add some figures.**

---

<sup>1</sup>For the general formula see [https://en.wikipedia.org/wiki/Curvature#Graph\\_of\\_a\\_function](https://en.wikipedia.org/wiki/Curvature#Graph_of_a_function)

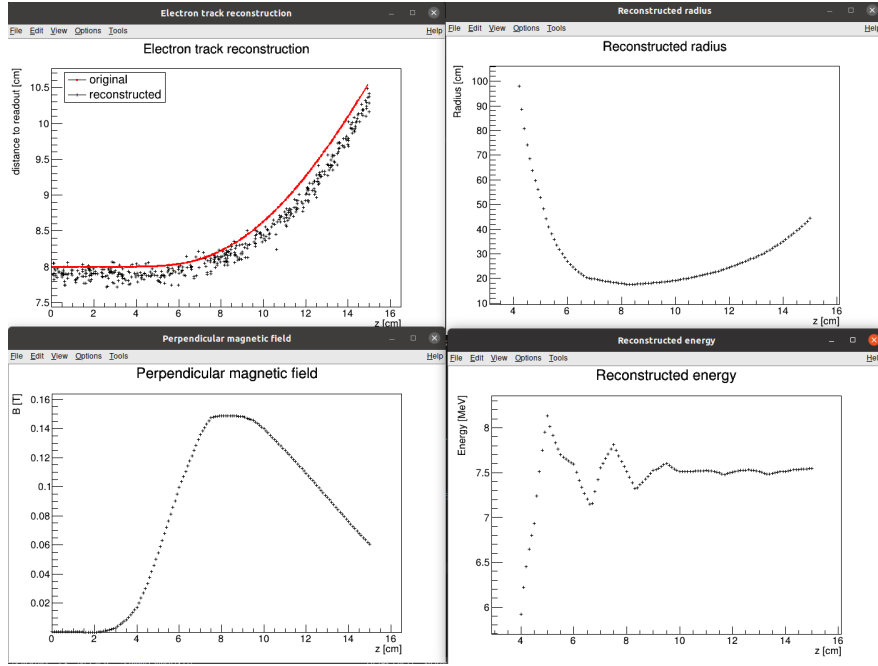


Figure 4.2: First attempt at a track reconstruction using only the drift velocity. Spline energy reconstruction attempt. Swap for better image(s) – subfigure environment, correct coordinates.

## 4.2 Circle and Lines Fit

Another way to estimate the particle’s kinetic energy is to fit its trajectory with a circular arc with lines attached smoothly. This shape of trajectory corresponds to a movement of a charged particle through a homogeneous magnetic field perpendicular to the particle’s momentum and limited to a certain volume. In general, the shape of such a trajectory in a non-perpendicularly oriented field is a spiral. In our case, this component is negligible since the field is approximately toroidal and the particle motion is nearly perpendicular to it. At first, we tested a 2D version of this fit, then we adapted it to 3D.

Our field is not homogeneous, it is therefore not entirely clear what value of magnetic field should be used along with the fitted radius (using equations 4.7 and 4.8) to get the best estimate for the kinetic energy. Since we only use this method as the first iteration of the particle’s energy that we later refine, an optimal solution of this problem is not required. Instead, we tested two options: taking the value of the field in the middle of the fitted circular arc and taking the average field along it. We haven’t really tried to plot this for multiple tracks, but these estimates are saved somewhere and could be plotted.

### 4.2.1 Two-dimensional fit

In the 2D case, the fitted function used for the electron track<sup>2</sup> described in Section 4.1 is defined as follows: Maybe describe this track that we used at the beginning somewhere earlier (section microscopic simulations → Testing track?) so that it is easier to refer to it in multiple sections. It is not part of the early GitHub

<sup>2</sup>Electron tracks bend towards negative  $z$ , we need to use the upper part of the circle

commits, so maybe it won't be possible to create exact replicas of the images, but they should be at least very similar.

$$z(x) = \begin{cases} a_1x + b_1 & x < x_1 \\ z_0 + \sqrt{r^2 - (x - x_0)^2} & x_1 \leq x \leq x_2, \\ a_2x + b_2 & x > x_2 \end{cases} \quad (4.9)$$

where  $a_{1,2}$  and  $b_{1,2}$  are the parameters of the lines,  $(x_0, z_0)$  is the center of the circle,  $r$  is its radius, and  $(x_{1,2}, z_{1,2})$  are the coordinates of the function's nodes. That means we have 9 parameters ( $z_{1,2}$  are not used in the function) along with 2 continuity conditions and 2 smoothness conditions. For the fit, we use the coordinates of the nodes and the radius of the circle, which gives us 5 independent parameters (only the radius has to be larger than half of the distance between nodes). The continuity conditions (combined with the relations for  $z_{1,2}$ ) are as follows:

$$z_{1,2} = a_{1,2}x_{1,2} + b_{1,2} = z_0 - \sqrt{r^2 - (x_{1,2} - x_0)^2}. \quad (4.10)$$

The smoothness conditions are as follows:

$$a_{1,2} = \frac{x_0 - x_{1,2}}{\sqrt{r^2 - (x_{1,2} - x_0)^2}}. \quad (4.11)$$

Equation 4.10 gives us the values of  $b_{1,2}$

$$b_{1,2} = z_{1,2} - a_{1,2}x_{1,2}. \quad (4.12)$$

For the coordinates of the center of the circle, we can use the fact that the center has to lie on the axis of its chord. In other words, there is a value of a parameter  $t$  such that, using the parametric equation of the axis

$$\begin{pmatrix} x_0 \\ z_0 \end{pmatrix} = \begin{pmatrix} \frac{x_1+x_2}{2} \\ \frac{z_1+z_2}{2} \end{pmatrix} + t \begin{pmatrix} \frac{z_2-z_1}{2} \\ \frac{x_1-x_2}{2} \end{pmatrix}. \quad (4.13)$$

At the same time, the center has to be in a distance of  $r$  from the nodes:

$$(x_1 - x_0)^2 + (z_1 - z_0)^2 = r^2, \quad (4.14)$$

$$\left(\frac{x_1 - x_2}{2} + \frac{z_1 - z_2}{2}t\right)^2 + \left(\frac{z_1 - z_2}{2} + \frac{x_2 - x_1}{2}t\right)^2 = r^2, \quad (4.15)$$

$$\left(\left(\frac{x_2 - x_1}{2}\right)^2 + \left(\frac{z_2 - z_1}{2}\right)^2\right)t^2 + \left(\frac{x_2 - x_1}{2}\right)^2 + \left(\frac{z_2 - z_1}{2}\right)^2 - r^2 = 0. \quad (4.16)$$

Since our electron track bends towards negative  $z$  and  $x_2 > x_1$ , we only care about the solution with  $t > 0$

$$t = \sqrt{\frac{r^2}{\left(\frac{x_2-x_1}{2}\right)^2 + \left(\frac{z_2-z_1}{2}\right)^2} - 1}, \quad (4.17)$$

$$x_0 = \frac{x_1 + x_2}{2} + \frac{z_2 - z_1}{2} \sqrt{\frac{r^2}{\left(\frac{x_2-x_1}{2}\right)^2 + \left(\frac{z_2-z_1}{2}\right)^2} - 1}, \quad (4.18)$$

$$z_0 = \frac{z_1 + z_2}{2} - \frac{x_2 - x_1}{2} \sqrt{\frac{r^2}{\left(\frac{x_2-x_1}{2}\right)^2 + \left(\frac{z_2-z_1}{2}\right)^2} - 1}. \quad (4.19)$$

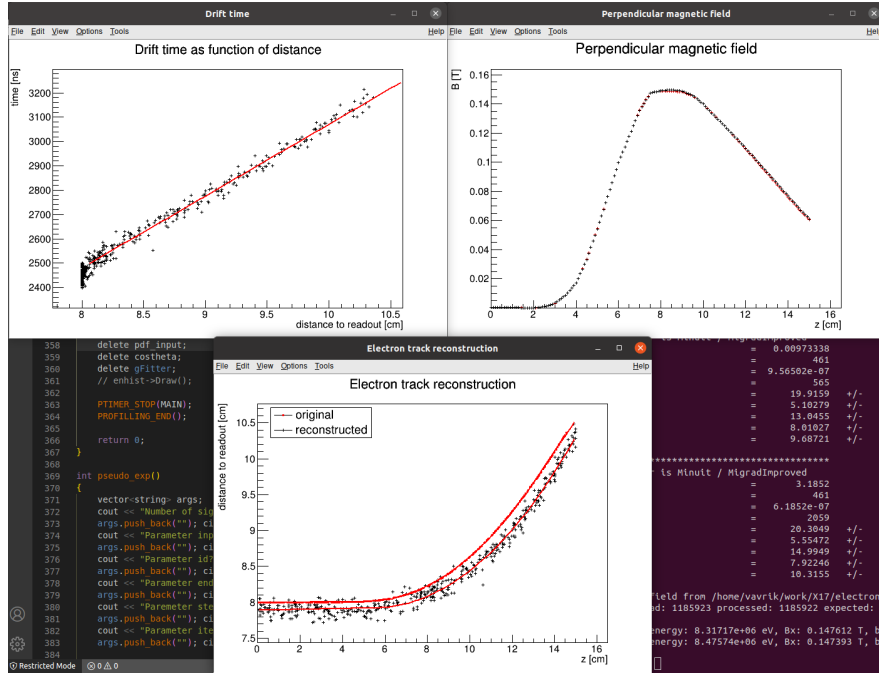


Figure 4.3: First attempt at a track reconstruction using only the drift velocity. Circle and Lines Fit in 2D. Swap for better image, correct coordinates.

692 The function defined in Equation 4.9 along with equations 4.11, 4.12, 4.18 and 4.19  
 693 derived using the continuity and smoothness conditions (combined with the re-  
 694 lations for  $z_{1,2}$ ) fully define our fitted function with parameters  $r, x_{1,2}, z_{1,2}$ . Some  
 695 pictures of the fit on the tested track. Results of the fit. Again, the actual fit  
 696 uses 8-z. Use GeoGebra schematics to generate a picture of 2D geometry.

697 Tested on a Runge-Kutta sample, and with microscopic tracks + map sim-  
 698 ulation. Preliminary 2D version (done) and complete 3D version. Geometry of  
 699 the fit with its derivation.

## 700 4.2.2 Three-dimensional fit

701 Explain the geometry and least square method used for the 3D fit.

## 702 4.3 Runge-Kutta Fit

703 Single parameter fit with 4th order Runge-Kutta simulated track. Future testing  
 704 with microscopic simulations and map simulation. Derivation of the geometry  
 705 (least squares).



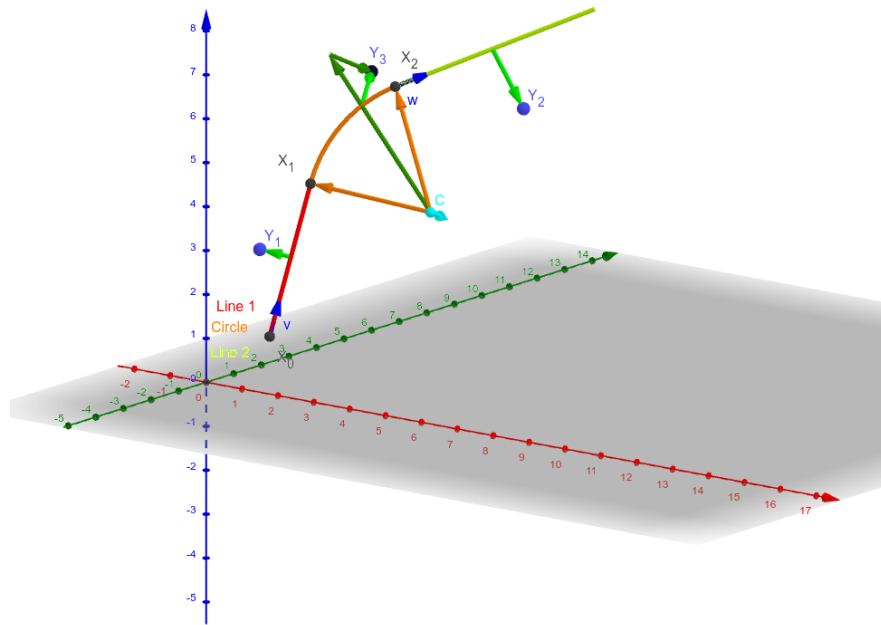


Figure 4.4: Circle and Lines Fit 3D geometry. [Swap for better image.](#)

# Conclusion

Here or at the end of each section. Something about the future of this work?

## Notes

General notes about the thesis:

- Check that all of the classes and other code are marked the same way in the text. I used italics somewhere, could use different font for this instead.
- Check unbreakable space in front of articles. Remove excessive article usage with proper nouns.
- Currently using margins for single-sided printing (bigger on the left side).
- Check that present tense is used
- American English quotation marks (") instead of British English (').
- Some of the overfull hbox warnings might change if duplex printing is used (they generate black rectangles on the edge of the page), leaving them be for now
- Check nobreakdash usage
- Check capitalized references (e.g., Figure, Section, Equation)
- Check  $\langle \dots \rangle$  math mode instead of  $\$ \dots \$$ . (actually unlike  $\langle \dots \rangle$  math mode, there is apparently no real benefit to this clumsy syntax)
- Use siunitx package to ensure correct formatting.
- Check other stuff that's written in the MFF UK template.
- Check correct subscripts in equation (italics vs no italics)

Random notes:

- Terminology consistency – ionization/primary/secondary electrons
- Only electrons that start and end in the sector closer than 0.5 cm are used for reconstruction (newest version).

## Future

Things planned for the future:

- Testing the reconstruction algorithm by measuring real particles with a known energy distribution.

- 735 • The **Fast Simulation with Ionization Electron Map** is planned for  
736 the future. It will use the HEED program [24] to simulate the primary par-  
737 ticle and the Ionization Electron Map (see Section 3.2) to simulate the drift  
738 of secondary electrons. It should be significantly faster than the Microscopic  
739 Simulation but offer comparable precision since it will rely on an already  
740 simulated drift map. (Primary track simulated in HEED. Readout paramet-  
741 ers by interpolating the map. Diffusion from the map for randomization.)
- 742 • Account for GEM, delta electrons, ...
- 743 • Likelihood approach instead of least squares (if it improves the reconstruc-  
744 tion significantly), we should at least use a better method than taking  
745 the center of the TPC bin.
- 746 • More detailed electric field simulation (if needed, GEM will have more com-  
747 plex field)

## 748 Likelihood - inverse map

749 If we wanted to further improve this procedure, taking into account the whole  
750 map  $\mathcal{M}$ , we could make an "inverse map" from  $\mathcal{R}$  to distributions on  $\mathcal{D}$ . We could  
751 achieve this by taking the normalized probability density of an electron with initial  
752 coordinates  $(x, y, z)$  having readout coordinates  $(x', y', t)$ . If we fix  $(x', y', t)$ , we  
753 get an unnormalized probability density  $f(x, y, z) = \mathcal{M}_{(x,y,z)}(x', y', t)$  (assuming  
754 that all initial coordinates are a priori equally likely). This could potentially  
755 improve the discrete reconstruction if we take the mean value of this probability  
756 density across the pad and time bin

$$f_{\text{pad, bin}}(x, y, z) = \frac{1}{A_{\text{pad}} \Delta t_{\text{bin}}} \int_{\text{pad, bin}} \mathcal{M}_{(x,y,z)}(x', y', t) dx' dy' dt \quad (4.20)$$

757 and using it for a likelihood fit instead of using least squares. This still assumes  
758 that all initial coordinates are equally likely which is clearly not the case for  
759 a primary particle track. In the future, we could even use the fast track simulation  
760 with the map (should be possible to make around 1000 tracks per minute per core  
761 with current settings), create a big set of tracks with reasonable parameters and  
762 use these to get an approximation of the probability distribution of the detector  
763 response. Some approximations would be necessary when interpreting the data to  
764 decrease the degrees of freedom of this distribution (we would have to pick a set of  
765 parameters and assume that some of them are independent). This could give us  
766 an idea about the best achievable resolution (how significantly will the detector  
767 response differ for a given change in energy). If the difference is significant, we  
768 could try to further improve the likelihood fit.

# Bibliography

- [1] Garfield++. <https://garfieldpp.web.cern.ch/garfieldpp/>. Accessed: 2023-05-18.
- [2] Rene Brun and Fons Rademakers. Root — An Object Oriented Data Analysis Framework. *Nuclear Instruments and Methods in Physics Research Section A: Accelerators, Spectrometers, Detectors and Associated Equipment*, 389(1–2):81–86, Apr 1997. Proceedings AIHENP’96 Workshop, Lausanne, Sep. 1996, See also <https://root.cern/>, Paper published in the Linux Journal, Issue 51, July 1998.
- [3] About MetaCentrum. <https://metavo.metacentrum.cz/en/about/index.html>, 2023. Accessed: 2024-11-27.
- [4] M. E. Rose. Internal Pair Formation. *Phys. Rev.*, 76:678–681, Sep 1949.
- [5] R. Essig, J. A. Jaros, W. Wester, P. Hansson Adrian, S. Andreas, T. Averett, O. Baker, B. Batell, M. Battaglieri, J. Beacham, T. Beranek, J. D. Bjorken, F. Bossi, J. R. Boyce, G. D. Cates, A. Celentano, A. S. Chou, R. Cowan, F. Curciarello, H. Davoudiasl, P. deNiverville, R. De Vita, A. Denig, R. Dharmapalan, B. Dongwi, B. Döbrich, B. Echenard, D. Espriu, S. Fegan, P. Fisher, G. B. Franklin, A. Gasparian, Y. Gershtein, M. Graham, P. W. Graham, A. Haas, A. Hatzikoutelis, M. Holtrop, I. Irastorza, E. Izaguirre, J. Jaeckel, Y. Kahn, N. Kalantarians, M. Kohl, G. Krnjaic, V. Kubarovsky, H-S. Lee, A. Lindner, A. Lobanov, W. J. Marciano, D. J. E. Marsh, T. Maruyama, D. McKeen, H. Merkel, K. Moffeit, P. Monaghan, G. Mueller, T. K. Nelson, G. R. Neil, M. Oriunno, Z. Pavlovic, S. K. Phillips, M. J. Pivovarov, R. Poltis, M. Pospelov, S. Rajendran, J. Redondo, A. Ringwald, A. Ritz, J. Ruz, K. Saenboonruang, P. Schuster, M. Shinn, T. R. Slatyer, J. H. Steffen, S. Stepanyan, D. B. Tanner, J. Thaler, M. E. Tobar, N. Toro, A. Upadye, R. Van de Water, B. Vlahovic, J. K. Vogel, D. Walker, A. Weltman, B. Wojtsekhowski, S. Zhang, and K. Zioutas. Dark Sectors and New, Light, Weakly-Coupled Particles, 2013.
- [6] F.W.N. de Boer, O. Fröhlich, K.E. Stiebing, K. Bethge, H. Bokemeyer, A. Balanda, A. Buda, R. van Dantzig, Th.W. Elze, H. Folger, J. van Klinken, K.A. Müller, K. Stelzer, P. Thee, and M. Waldschmidt. A deviation in internal pair conversion. *Physics Letters B*, 388(2):235–240, 1996.
- [7] F W N de Boer, R van Dantzig, J van Klinken, K Bethge, H Bokemeyer, A Buda, K A Müller, and K E Stiebing. Excess in nuclear pairs near 9 MeV/ invariant mass. *Journal of Physics G: Nuclear and Particle Physics*, 23(11):L85, nov 1997.
- [8] F W N de Boer, K Bethge, H Bokemeyer, R van Dantzig, J van Klinken, V Mironov, K A Müller, and K E Stiebing. Further search for a neutral boson with a mass around 9 MeV/c<sup>2</sup>. *Journal of Physics G: Nuclear and Particle Physics*, 27(4):L29, apr 2001.

- [9] Attila Vitéz, A. Krasznahorkay, J. Gulyas, Margit Csatos, Lorant Csige, Zoltan Gacsi, Barna Nyakó, F. Boer, T. Ketel, and J. Klinken. Anomalous Internal Pair Creation in  $^8\text{Be}$  as a Signature of the Decay of a New Particle. *Acta Physica Polonica B - ACTA PHYS POL B*, 39:483, 02 2008.
- [10] A. Krasznahorkay, J. Gulyas, Margit Csatos, Attila Vitéz, T. Tornyai, L. Stuhl, Lorant Csige, Zoltan Gacsi, A. J. Krasznahorkay, M. Hunyadi, and T.J. Ketel. Searching for a light neutral axial-vector boson in isoscalar nuclear transitions. *Frascati Physics Series*, 56:86, 10 2012.
- [11] A. J. Krasznahorkay, M. Csatlós, L. Csige, Z. Gács, J. Gulyás, M. Hunyadi, I. Kuti, B. M. Nyakó, L. Stuhl, J. Timár, T. G. Tornyai, Zs. Vajta, T. J. Ketel, and A. Krasznahorkay. Observation of Anomalous Internal Pair Creation in  $^8\text{Be}$ : A Possible Indication of a Light, Neutral Boson. *Physical Review Letters*, 116(4), January 2016.
- [12] D.R. Tilley, J.H. Kelley, J.L. Godwin, D.J. Millener, J.E. Purcell, C.G. Sheu, and H.R. Weller. Energy levels of light nuclei  $A=8,9,10$ . *Nuclear Physics A*, 745(3):155–362, 2004.
- [13] N. J. Sas, A. J. Krasznahorkay, M. Csatlós, J. Gulyás, B. Kertész, A. Krasznahorkay, J. Molnár, I. Rajta, J. Timár, I. Vajda, and M. N. Harakeh. Observation of the X17 anomaly in the  $^7\text{Li}(p,e^+e^-)^8\text{Be}$  direct proton-capture reaction, 2022.
- [14] A. J. Krasznahorkay, M. Csatlós, L. Csige, J. Gulyás, A. Krasznahorkay, B. M. Nyakó, I. Rajta, J. Timár, I. Vajda, and N. J. Sas. New anomaly observed in  $^4\text{He}$  supports the existence of the hypothetical X17 particle. *Physical Review C*, 104(4), October 2021.
- [15] D.R. Tilley, H.R. Weller, and G.M. Hale. Energy levels of light nuclei  $A = 4$ . *Nuclear Physics A*, 541(1):1–104, 1992.
- [16] A. J. Krasznahorkay, A. Krasznahorkay, M. Begala, M. Csatlós, L. Csige, J. Gulyás, A. Krakó, J. Timár, I. Rajta, I. Vajda, and N. J. Sas. New anomaly observed in  $^{12}\text{C}$  supports the existence and the vector character of the hypothetical X17 boson. *Phys. Rev. C*, 106:L061601, Dec 2022.
- [17] F. Ajzenberg-Selove. Energy levels of light nuclei  $A = 11,12$ . *Nuclear Physics A*, 506(1):1–158, 1990.
- [18] Péter Kálmán and Tamás Keszthelyi. Anomalous internal pair creation. *The European Physical Journal A*, 56, 08 2020.
- [19] A. Aleksejevs, S. Barkanova, Yu. G. Kolomensky, and B. Sheff. A Standard Model Explanation for the "ATOMKI Anomaly", 2021.
- [20] Jonathan L. Feng, Bartosz Fornal, Iftah Galon, Susan Gardner, Jordan Smolinsky, Tim M. P. Tait, and Philip Tanedo. Protophobic Fifth-Force Interpretation of the Observed Anomaly in  $^8\text{Be}$  Nuclear Transitions. *Phys. Rev. Lett.*, 117:071803, Aug 2016.

- [21] Tran The Anh, Tran Dinh Trong, Attila J. Krasznahorkay, Attila Krasznahorkay, József Molnár, Zoltán Pintye, Nguyen Ai Viet, Nguyen The Nghia, Do Thi Khanh Linh, Bui Thi Hoa, Le Xuan Chung, and Nguyen Tuan Anh. Checking the  $8\text{Be}$  Anomaly with a Two-Arm Electron Positron Pair Spectrometer. *Universe*, 10(4):168, April 2024.
- [22] Kh. U. Abraamyan, Ch. Austin, M. I. Baznat, K. K. Gudima, M. A. Kozhin, S. G. Reznikov, and A. S. Sorin. Observation of structures at  $\sim 17$  and  $\sim 38$   $\text{MeV}/c^2$  in the  $\gamma\gamma$  invariant mass spectra in pC, dC, and dCu collisions at  $p_{lab}$  of a few  $\text{GeV}/c$  per nucleon, 2023.
- [23] The MEG II collaboration, K. Afanaciev, A. M. Baldini, S. Ban, H. Benmansour, G. Boca, P. W. Cattaneo, G. Cavoto, F. Cei, M. Chiappini, A. Corvaglia, G. Dal Maso, A. De Bari, M. De Gerone, L. Ferrari Barusso, M. Francesconi, L. Galli, G. Gallucci, F. Gatti, L. Gerritzen, F. Grancagnolo, E. G. Grandoni, M. Grassi, D. N. Grigoriev, M. Hildebrandt, F. Ignatov, F. Ikeda, T. Iwamoto, S. Karpov, P. R. Kettle, N. Khomutov, A. Kolesnikov, N. Kravchuk, V. Krylov, N. Kuchinskiy, F. Leonetti, W. Li, V. Malyshev, A. Matsushita, M. Meucci, S. Mihara, W. Molzon, T. Mori, D. Nicolò, H. Nishiguchi, A. Ochi, W. Ootani, A. Oya, D. Palo, M. Panareo, A. Papa, V. Pettinacci, A. Popov, F. Renga, S. Ritt, M. Rossella, A. Rozhdestvensky. S. Scarpellini, P. Schwendimann, G. Signorelli, M. Takahashi, Y. Uchiyama, A. Venturini, B. Vitali, C. Voena, K. Yamamoto, R. Yokota, and T. Yonemoto. Search for the X17 particle in  ${}^7\text{Li}(p, e^+e^-){}^8\text{Be}$  processes with the MEG II detector, 2024.
- [24] I.B. Smirnov. Modeling of ionization produced by fast charged particles in gases. *Nuclear Instruments and Methods in Physics Research Section A: Accelerators, Spectrometers, Detectors and Associated Equipment*, 554(1):474–493, 2005.
- Acknowledgments:** Computational resources were provided by the e-INFRA CZ project (ID:90254), supported by the Ministry of Education, Youth and Sports of the Czech Republic.

# List of Figures

880			
881	1	The ATOMKI anomalous IPC measured for different nuclei. . . .	4
882	2	Results from the Hanoi spectrometer – angular $e^+e^-$ pair correlations measured in the ${}^7\text{Li}(p, e^+e^-){}^8\text{Be}$ reaction at $E_p = 1225$ keV [21].	5
883			
884	3	Results from the MEG II experiments – angular correlation of $e^+e^-$ pairs with $E_{\text{sum}} \in [16, 20]$ MeV measured in the ${}^7\text{Li}(p, e^+e^-){}^8\text{Be}$ reaction with proton beam energies 500 and 1080 keV. The 500 keV dataset is fitted with Monte Carlo of both the IPC deexcitation and the EPC produced by gammas [23]. . . . .	6
885			
886			
887			
888			
889	1.1	Pad layout of the TPC. <b>Swap for better image.</b> . . . . .	11
890	1.2	Visualization of trilinear interpolation as a composition of linear interpolations. <b>Image drawn in GeoGebra and inspired by a similar image on Wikipedia (which looks a bit worse) – is credit necessary?</b>	12
891			
892			
893	2.1	Example of a simulated electron track in 70 % argon and 30 % $\text{CO}_2$ atmosphere (on the left). <b>Swap for better images, better zoom. Explain drift lines, primary particle.</b> . . . . .	14
894			
895			
896	2.2	Comparison of diffusion in a simulated electron track in 70 % argon, 30 % $\text{CO}_2$ atmosphere and in 90 % argon, 10 % $\text{CO}_2$ atmosphere (on the right). <b>Swap for better image, better zoom. Or put the same pictures for both comparisons in one subfigure, etc. Describe better.</b> . . . . .	14
897			
898			
899			
900			
901	3.1	Dependence of the drift time on the $z$ coordinate in 90 % argon and 10 % $\text{CO}_2$ atmosphere, fitted with a linear function. The fitted function gives us the average drift velocity in the gas and can be used for rough reconstruction in our TPC. <b>Swap for better image with axis labels, etc. Maybe write the fitted equation.</b> . . . . .	16
902			
903			
904			
905			
906	3.2	First attempt at a track reconstruction using only the drift velocity. This approach works well in a standard TPC ( <b>ideally cite some source?</b> ). 90 % argon and 10 % $\text{CO}_2$ atmosphere. <b>Swap for better image, correct coordinates.</b> . . . . .	17
907			
908			
909			
910	3.3	First attempt at a track reconstruction using only the drift velocity, residues. <b>Swap for better image, correct coordinates. What's causing the shift? Explain details.</b> . . . . .	17
911			
912			
913	3.4	Example of map generation. <b>Swap for better image, correct coordinates.</b> . . . . .	19
914			
915	3.5	Example reconstruction with the map. <b>Swap for better image, correct coordinates.</b> . . . . .	20
916			
917	3.6	Selection of the points for interpolation. <b>Create better images; use the explanation interpolation vs. extrapolation strange property. Solution 2 probably does not make much sense.</b> . . . . .	22
918			
919			
920	4.1	Example of a fitted reconstructed track. <b>Swap for better image.</b> .	24
921	4.2	First attempt at a track reconstruction using only the drift velocity. Spline energy reconstruction attempt. <b>Swap for better image(s) – subfigure environment, correct coordinates.</b> . . . . .	26
922			
923			

924	4.3	First attempt at a track reconstruction using only the drift velocity.	
925		Circle and Lines Fit in 2D. <a href="#">Swap for better image, correct</a>	
926		<a href="#">coordinates.</a> . . . . .	28
927	4.4	Circle and Lines Fit 3D geometry. <a href="#">Swap for better image.</a> . . . . .	29



# 928 List of Tables

# 929 List of Abbreviations

930 **GEM** Gas Electron Multiplier

931 **HEED** High Energy Electro-Dynamics

932 **IEAP CTU** Institute of Experimental and Applied Physics, Czech Technical  
933 University in Prague

934 **IPC** Internal Pair Creation

935 **EPC** External Pair Creation

936 **Micromegas** MICRO-MESh Gaseous Structure

937 **MWPC** Multi-Wire Proportional Chamber

938 **OFTPC** Orthogonal Fields TPC

939 **TPC** Time Projection Chamber

940 **ToA** time-of-arrival

941 **ToT** time-over-threshold

942 **Tpx3** Timepix 3